博士論文

Development of a high finesse optical cavity with self-resonating mechanism for laser Compton scattering sources

（レーザーコンプトン散乱光源のための高フィネス自発共鳴型光共振器の開発）

上杉　祐貴

広島大学大学院先端物質科学研究科

2016年5月

目次

１．主論文

Development of a high finesse optical cavity with self-resonating mechanism for laser Compton scattering sources

（レーザーコンプトン散乱光源のための高フィネス自発共鳴型光共振器の開発）

上杉　祐貴

２．公表論文

(1) Feedback-free optical cavity with self-resonating mechanism
Y. Uesugi, Y. Hosaka, Y. Honda, A. Kosuge, K. Sakaue, T. Omori, T. Takahashi, J. Urakawa and M. Washio
APL Photonics **1**, 026103-1-7 (2016); doi: 10.1063/1.4945353

３．参考論文

(1) Demonstration of the Stabilization Technique for Nonplanar Optical Resonant Cavities Utilizing Polarization
T. Akagi, S. Araki, Y. Funahashi, Y. Honda, S. Miyoshi, T. Okugi, T. Omori, H. Shimizu, K. Sakaue, T. Takahashi, R. Tanaka, N. Terunuma, Y. Uesugi, J. Urakawa, M. Washio and H. Yoshitama
Review of Scientific Instruments **86**, 043303-1-7 (2015); doi: 10.1063/1.4918653

(2) Development of an intense positron source using a crystal-amorphous hybrid target for linear colliders
Y. Uesugi, T. Akagi, R. Chehab, O. Dadoun, K. Furukawa, T. Kamitani, S. Kawada, T. Omori, T. Takahashi, K. Umemori, J. Urakawa, M. Satoh, V. Strakhovenko, T. Suwada and A. Variola
Nuclear Instruments and Methods in Physics Research B, **319**, 17-23 (2014); doi:10.1016/j.nimb.2013.10.025

主論文

Development of a high finesse optical cavity with self-resonating mechanism for laser Compton scattering sources

Graduate School of Advanced Sciences of Matter,

Hiroshima University

Yuuki UESUGI

20 May 2016

Abstract

We developed a high finesse optical cavity without utilizing an active feedback system to stabilize the resonance aiming for light sources with laser Compton scattering. Laser Compton scattering is the elastic scattering process of laser photons and high energy electrons. It generates X-rays or gamma-rays with relatively low energy electron beams compared with synchrotron radiation and allow us to construct compact photon source facilities. X-ray sources are useful for commercial, medical applications and material science, and gamma-ray sources are used for nuclear and particle physics. For example, a Compton based polarized positron source is considered as a possible option for the polarized positron source for the International Linear Collider (ILC).

A challenge for laser Compton scattering light sources is to improve their brightness. Therefore, laser photon density at the interaction point of the laser photons and the electrons must be increased. We have focused to increase the intensity of the laser photons by utilizing an optical resonant cavity to accumulate pulsed laser coherently. In the previous study, we developed the cavity which had the finesse of 4,040, the power enhancement factor of 1,280 and the focal spot size of $10 \times 27\ \mu m$. With the laser power accumulation in the cavity which was 2.6 kW during the experiment, the gamma-ray generation was performed with the 1.28 GeV electron beam at High Energy Accelerator Research Organization (KEK) in 2013. The gamma-ray production rate was achieved at 2.7×10^8 photons/sec.

For practical applications, more power enhancement is required to increase the number of generated photons, however, a technical difficulty lies in the improvement of the feedback control system as the linewidth of cavity resonance is inversely proportional to the finesse. In this work, a feedback-free optical cavity with self-resonating mechanism has been developed to overcome this problem. The highly stable operation with the effective finesse of $394,000 \pm 10,000$, the power enhancement factor of $187,000 \pm 1,000$ and the stored laser power of 2.52 ± 0.13 kW with the stability of 1.7 % were successfully demonstrated. The obtained effective finesse and power stability correspond to the stabilizing accuracy of 0.16 pm in the cavity length.

This study showed the possibility of realizing a high finesse cavity without any sophisticated active feedback system which, in principle, overcomes issues of the stabilization of optical resonant cavities with an active feedback control, if the application will not require narrow bandwidth in the light frequency. The feedback-free optical cavity is highly useful for applications, such as photon facilities by laser-Compton scattering or highly sensing applications like cavity enhanced absorption spectroscopy (CEAS).

Acknowledgements

This thesis could not have been written without the help and support from many people.

Firstly, I would like to express my gratitude to my supervisor Dr. T. Takahashi of Hiroshima University.

I am particularly grateful to the members of the LCSS development group and all collaborators: Prof. Junji Urakawa, Dr. T. Omori, Dr. Y. Honda, Dr. A. Kosuge, Dr. T. Akagi and Dr. M. Fukuda of High Energy Accelerator Research Organization (KEK), Prof. M. Washio, Dr. K. Sakaue and Y. Hosaka of Waseda University, Dr. D. Tatsumi and Dr. A. Ueda of National Astronomical Observatory of Japan (NAOJ), and Dr. H. Yoshitama and R. Tanaka. Without the generous help of these individuals, this work of true passion would not have been possible.

I would like to acknowledge to the members of Hiroshima University and the students studied together: Dr. M. Iinuma, Prof. M. Kuriki, Dr. S. Kawada, Y. Suzuki, M. Miyamoto, A. Yokota, M. Urano and others. The fruitful discussions with them helped me a lot in understanding the various aspects of physics. And also Dr. H. Iijima, Dr. Y. Seimiya and Dr. K. Negishi are not the current members of Hiroshima University but I would like thank to their helpful and clerical support.

Lastly, I would like to thank my parents for their continuous support.

Yuuki UESUGI
March 22, 2016
Hiroshima, Japan

Contents

List of Figures

List of Tables

Chapter 1

Introduction

1.1 Motivation

Laser Compton scattering is a noble method to generate polarized photons in the energy from X-ray to gamma-ray region by elastic scattering of laser photons and high energy electrons. It is expected that the process will be utilized as X-ray sources for industrial, medical or material science, and gamma-ray sources for high energy or nuclear physics [1–4]. In generally, X-ray sources used in microstructure analyses is formed by synchrotron radiation facilities or recently by free electron laser facilities; these sources require a large scale facility because they need several GeV electron beams. On the other hand, the laser Compton scattering source can save a footprint and costs since the required electron energy to generate the same energy X-rays by laser Compton scattering is lower than one required by the synchrotron radiation. For instance, hard X-rays with the energy of $O(10)$ keV can be produced by $O(10)$ MeV electrons with 1 μm wavelength laser light.

Furthermore, the laser Compton scattering source has an advantage of being able to control the polarization of the photons by changing the polarization of the laser light. The laser Compton scattering source is a candidate to construct a polarized positron sources for linear colliders and a proof-of-principle of the generation of polarized positrons by polarized gamma-rays has been performed [5–7]. If one generates the gamma-rays by synchrotron radiation, the electron energy of about 150 GeV is required in order to produce the about 10 MeV gamma-ray which is required to generate positrons via the electron-positron pair production process. The International Linear Collider (ILC) [8–12], which is a next-generation electron-positron collider with the total length of about 31 km and the center-of-mass energy of up to 500 GeV, requires the gamma-ray driven polarized positron source. In the design report of the ILC positron source, the gamma-rays are generated by an undulator which has the length of 200 m and requires 150 GeV electron beam from the main linac of the ILC. That scheme is expected to generate the positrons with the polarization ratio of about 30 % at its initial operation and expected to be upgradable to 60 %. As the future plan, the design report also shows another polarized positron source scheme which is driven by the laser Compton scattering gamma-ray source since this scheme can generate the10 MeV gamma-ray with only 1 GeV electron beams and has higher polarization and more flexibility for polarization switching than the undulator scheme.

The most important subject for many practical uses of the laser Compton scattering source is increases of the brightness of the X-rays or gamma-rays. It is possible to increase the yields of scattered photons by inserting an optical resonant cavity into the electron storage ring [13], so we have developed the optical cavity and carried out gamma-ray generation experiments with 1.28 GeV electron beams at the Advanced Test Facility of the High Energy Accelerator Research Organization (KEK) in Japan [14–18]. The optical cavity can accumulate laser pulses coherently and increases the laser power with the enhancement factor of F/π, where F is the finesse that is a parameter indicating the sharpness of the resonance. In addition, the cavity also can focus the laser light down to a few 10 micrometers at the focal point in the cavity. Firstly, we developed a Fabry-Pérot cavity with the finesse of about 1,000, the enhancement factor of 250 and the focal spot size of 60 μm. The average storage power of 498 W was achieved with 10 W picosecond pulsed laser source [15]. In the second experiment, the 3 dimensional 4 mirror optical cavity with the finesse of 4,040, the enhancement factor of 1,280 and the elliptical focal spot of 10×27 μm was developed. By accumulating laser with 2.6 kW average power in that cavity, the gamma-ray generation with 2.7×10^8 photons/sec was achieved [17].

For practical applications, more number of scattered photons are needed than the one obtained in our recent experimental results. A reliable way to improve the brightness is to increase the cavity finesse. However, such high finesse cavity follows a technical difficulty on maintaining the resonance condition of the cavity because the linewidth of the resonance is inversely proportional to the finesse. To accumulate laser light coherently in the cavity, the resonance condition of

$$L_{cav} = q\lambda \tag{1.1.1}$$

must be satisfied, where L_{cav}, q, and λ are one round-trip pass length in the cavity, an integer, and the wavelength of the incident laser light, respectively. For example, the optical pass length of our cavity was stabilized by a feedback controller with piezo-electric devices [16–18]. The finesse of it was 4,040 and the achieved accuracy of the optical pass length in order to maintain the resonance was 16 pm. If one assumes the cavity finesse of 40,000, the resonance linewidth in the full width half mean will be about 25 pm. And the accuracy required to stabilize the resonance at the same level as the $F = 4{,}040$ condition is less than a picometer. This requirement may be achievable [19] but potentially has technical challenges.

1.2 A feedback-free optical cavity with self-resonating mechanism

Recently, we developed a new laser storage system which can avoid the issue of stabilization which maintains the resonance condition. That cavity system has mechanism to maintain the resonance in itself, hence there is no problem caused by feedback control. The idea of "self-resonating mechanism" was proposed by Y. Honda and K. Sakaue in 2010 [20]. Figure 1.1 shows a conceptual drawing of the feedback-free cavity with self-resonating mechanism. Since it is composed of an optical amplifier and an optical resonant cavity through optical loop pass, it also can be regarded as a kind of laser oscillator. Laser oscillators including optical resonator (or etalon) in the loop path has been widely used as a technique to stabilize laser operation e.g. [21, 22], however, none of them have focused on stabilizing the resonance of the cavity and utilizing the enhance laser power in it.

The principle of operation of this system is explained below. Amplified spontaneous emission (ASE) light with a wide frequency spectrum would be emitted from the optical amplifier and is incident on the optical resonant cavity. A part of the light which satisfy the resonance condition of the cavity accumulates in the cavity and passes through without optical loss. The leaked light from the cavity comes back to the amplifier and is amplified coherently as the seed light, hence the system will reach laser oscillation if the gain exceeds power losses in the entire optical loop. At that time, the laser power in the cavity will be enhanced by the factor determined by the cavity finesse. If the cavity length fluctuates due to external disturbances in the environment, the resonance frequency of the cavity is also fluctuate. However, the optical frequency of the laser oscillation is always caused by the frequency of the cavity mode, hence the system will maintain the laser oscillation, the resonance condition and the laser storage in principle.

Practically, the operating behavior of the feedback-free cavity would depend on various conditions such as the pump rate, the lifetime of the excited state in the lasing media, losses in the optical loop, the strength of the external disturbances, the mechanical vibration property of the cavity, etc. In order to evaluate the possibility to utilize that cavity system for laser Compton scattering sources, the stable laser storage in the case of high finesse and the realization of the mode-locking to produce short laser pulse should be examined experimentally.

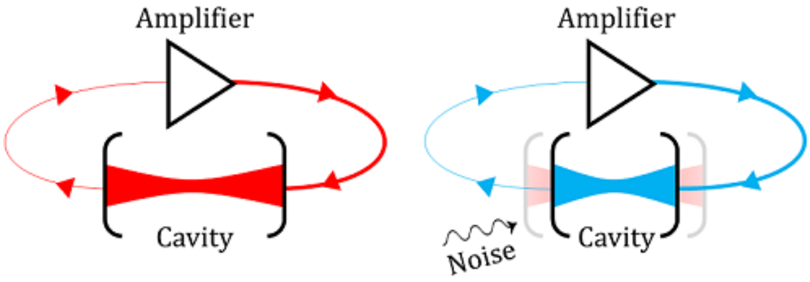

Figure 1.1: A conceptual drawing of a feedback-free optical cavity with self-resonating mechanism. The detail is in the main text.

1.3 Focus of Dissertation

In this thesis, the development of a feedback-free optical resonant cavity with high finesse (394,000) in continuous oscillation operation is introduced. That finesse is two orders of magnitude higher than one of our previous performance. Thanks to the self-resonant mechanism, the demonstration of maintaining the resonance was proven successfully even without high precision electronic circuits or special quiet environment.

In order to provide basic knowledge about a laser Compton scattering source, an optical power enhancement cavity and a laser oscillator, the theoretical background is introduced in Chapter 2. High quality optical mirrors enabling the large power enhancement and evaluation methods of performance of the cavity are introduced in Chapter 3. Chapter 4 shows the results of the principle verification experiment using a low finesse cavity and the demonstration of the stable laser storage with the power enhancement factor of mort than 100,000. Chapter 5 is a conclusion of this thesis.

Chapter 2

Theoretical backgrounds

2.1 Laser Compton scattering and scattered photon beam

The laser Compton scattering means Compton scattering process with laser photons and high energy electrons. The laser photon energy is around visible range of $O(1)$ eV while the electron have relativistic energy. Many theoretical studies and numerical simulations for light sources using the laser Compton scattering have been conducted so far (e.g. [23–26]). In this section, the characteristics of scattered photons due to Compton scattering are introduced; where by taking account the photon energy range of many practical X-ray or gamma-ray sources, the recoil effect has been neglected.

2.1.1 Photon generation by Compton scattering

Consider an electron and a photon in a laboratory frame coordinate system (x, y, z) as shown in the geometry of the scattering, figure 2.1. The 4-momenta of the initial and final electrons are defined as $p = (E_e/c,\ \vec{p})$ and $p' = (E'_e/c,\ \vec{p'})$, where c is the speed of light. The initial electron is moving along the z direction. The 4-momenta of the incident and scattered photons are defined as $k = (E_p/c,\ \hbar\vec{k})$ and $k' = (E'_p/c,\ \hbar\vec{k'})$, where $\hbar$ is the Planck constant. The incident photon is propagated along the direction with the elevation angle θ_i and azimuth angle ϕ_i, and the scattered photon

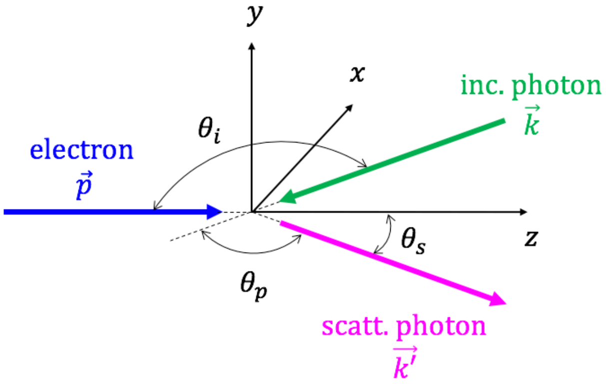

Figure 2.1: Geometry of Compton scattering in a laboratory frame coordinate system (x, y, z). The final electron p' which is the electron after scattering is not shown in this figure. The detail is in the main text.

is propagated along the direction with θ_s and ϕ_s. The angle θ_p $(= \theta_i - \theta_s)$ in figure 2.1 is the angle between the momenta of the incident and scattered photons.

The energy of the scattered photon can be obtained from the kinematic relation between the electrons and photons:

$$p + k = p' + k'. \tag{2.1.1}$$

Squaring both side of this equation, we can obtain

$$E'_p = \frac{1 - \beta \cos \theta_i}{1 - \beta \cos \theta_s + \varepsilon(1 - \cos \theta_p)} E_p, \tag{2.1.2}$$

where $\beta = v/c$, v is the velocity of the initial electron, and ε is the ratio between the energies of the initial electron and the incident photon:

$$\varepsilon = \frac{E_p}{E_e}. \tag{2.1.3}$$

Figure 2.2 shows the relation between the scattered photon energy and the scattering angle with the incident angle of 180° (line), 120° (dash) and 90° (dots). The scattered angle θ_s is normalized with a factor of γ; position 1 on the horizontal axis shows the scattered angle of $\theta_s = 1/\gamma$ [rad]. Those plots are calculated with the electron energy of 1.28 GeV and the wavelength of the incident laser of 1064 nm. It is found that the higher energy photons are

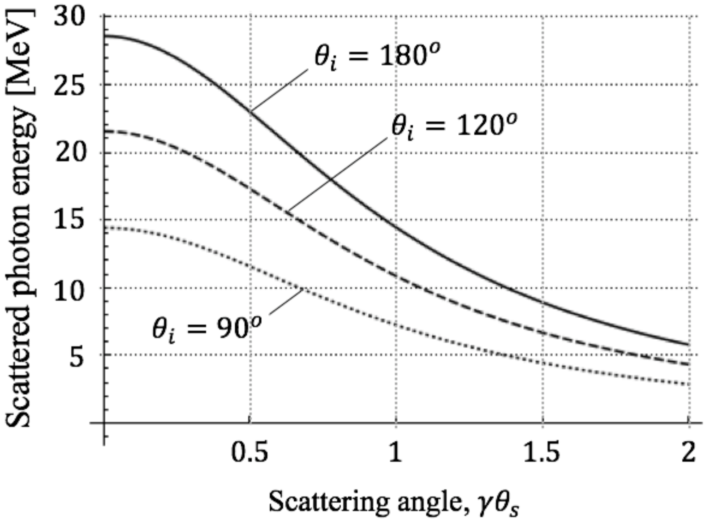

Figure 2.2: Scattered photon energy as a function of the scattered angle. The electron energy and the wavelength of the incident laser are 1.28 GeV and 1064 nm, respectively. Each curve correspond to the incident angle of 180° (line), 120° (dash) and 90° (dots).

concentrated around the axis of the electron propagation, $\theta_s = 0$, regardless of the incident angle.

In the head-on collision case, $\theta_i = \pi$, equation (2.1.2) can be rewritten as

$$E'_p = \frac{1+\beta}{1-\beta\cos\theta_s + \varepsilon(1+\cos\theta_s)} E_p. \tag{2.1.4}$$

Furthermore, assuming that the electron's velocity is almost close to the speed of light, the scattered photon energy in a small scattered angle, $\theta_s \ll 1$, is given by

$$E'_p = \frac{4\gamma^2}{1+4\gamma^2\varepsilon} E_p, \tag{2.1.5}$$

where $\gamma = 1/\sqrt{1-\beta^2}$ is the Lorentz factor of the initial electron. Neglecting the recoil effect is a good assumption for practical applications of X-ray or relatively low energy gamma-ray sources: $4\gamma^2\varepsilon \ll 1$. Taking account these assumption, the approximate maximum energy of scattered photons is given by

$$E'_p \sim 4\gamma^2 E_p. \tag{2.1.6}$$

This result shows that the incident photon is boosted by a factor of about γ^2. Since the Lorentz factor of the electron γ is much bigger than unity in the ultra-relativistic case, the laser Compton scattering using an electron accelerator can be utilized to produce high-energy photons even though laser photons are only $O(1)$ eV energy.

2.1.2 Energy spectrum of scattered photons

The energy spectrum of the scattered photons is important to estimate the number of high-energy scattered photons obtained by the Compton scattering. The differential cross section of Compton scattering for unpolarized electrons and photons is given by [23]

$$\frac{d\sigma}{dY d\phi_s} = \frac{4r_e^2}{X^2}\left[\left(\frac{1}{X}-\frac{1}{Y}\right)^2+\frac{1}{X}-\frac{1}{Y}+\frac{1}{4}\left(\frac{X}{Y}+\frac{Y}{X}\right)\right], \tag{2.1.7}$$

where ϕ_s is the azimuthal angle of the scattered photon; r_e is the classical electron radius; and X and Y are the relativistic invariant variables defined as [27]

$$X = \frac{(p+k)^2 - m^2c^2}{m^2c^2}, \quad Y = \frac{m^2c^2 - (p-k')^2}{m^2c^2}. \tag{2.1.8}$$

In the head-on collision case, $\theta_i = \pi$, these variables are rewritten as

$$X = \frac{2\gamma E_p(1+\beta)}{mc^2}, \quad Y = \frac{2\gamma E'_p(1-\beta\cos\theta_s)}{mc^2}, \tag{2.1.9}$$

where it should be denoted that $\cos\theta_s$ is a function of the scattered photon energy E'_p through equation (2.1.4).

We can obtain dY as follows [25]:

$$\begin{aligned} Y &= X\frac{\beta E_e - E'_p}{\beta E_e - E_p}, \\ \therefore\ dY &= -X\frac{dE'_p}{\beta E_e - E_p}. \end{aligned} \tag{2.1.10}$$

Substituting dY in equation (2.1.7) and integrating on the azimuthal angle ϕ_s, the energy distribution of the scattered photons is obtained as

$$\frac{d\sigma}{dE'_p} = \frac{8\pi r_e^2}{X^2(\beta E_e - E_p)}\left[\left(\frac{1}{X}-\frac{1}{Y}\right)^2+\frac{1}{X}-\frac{1}{Y}+\frac{1}{4}\left(\frac{X}{Y}+\frac{Y}{X}\right)\right]. \tag{2.1.11}$$

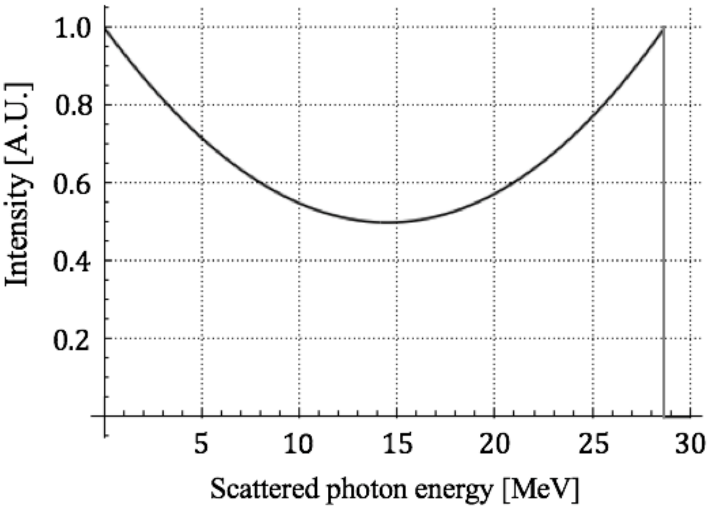

Figure 2.3: The energy spectrum of the scattered photons by Compton scattering with the electron energy of 1.28 GeV and the laser wavelength of 1064 nm.

The energy spectrum of the scattered photons with the electron energy of 1.28 GeV and the laser wavelength of 1064 nm is shown in figure 2.3. The spectral intensity has a maximum value at the scattered photon energy of about 29 MeV, which is the maximum energy obtained at the scattered angle of $\theta_s = 0$. And a minimum value at the scattered photon energy of about 15 MeV, that energy is obtained at the scattered angle of $\theta_s = 1/\gamma$ according to the angular distribution of the scattered photon energy, figure 2.2. Thus, a half of power of the scattered photons will be concentrated in a cone of the angle $\theta_s = 1/\gamma = 0.399$ [mrad]. The results indicates that we can obtain a high-energy scattered photon beam with a small energy spread by using collimators at downstream of the interaction area.

2.1.3 Flux of a scattered photon beam

To obtain the expression for the total flux of the scattered photons, consider the beam-beam scattering of the electrons and laser photons. Figure 2.4 shows the collision of a bunched electron beam and a pulsed laser beam in a laboratory frame coordinate system (x, y, z). The electron bunch is moving

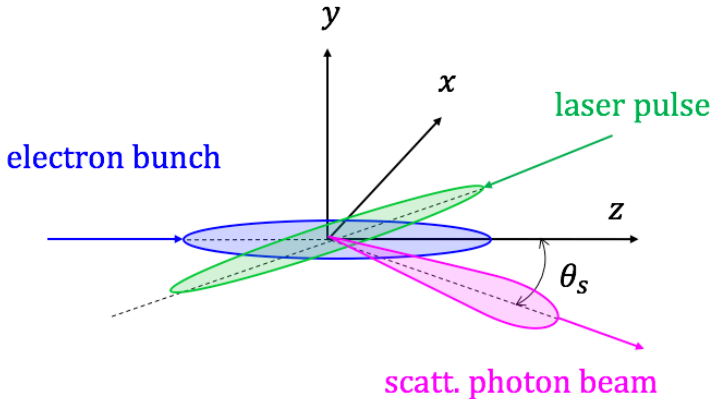

Figure 2.4: Geometry of the beam-beam scattering in a laboratory frame coordinate system (x,y,z). The detail is in the main text.

along the z direction, the time origin $t = 0$ is chosen for the instant when the center of the electron bunch and laser pulse collide, and the spatial origin is chosen that interaction center position.

The number of scattered photons during the fraction of time in the fraction of a phase space volume of the electron bunch and laser pulse is given by

$$dN(\vec{r},\vec{p},\vec{k},t) = \sigma_t(\vec{p},\vec{k})\, N_e f_e(\vec{r},\vec{p},t)\, N_p f_p(\vec{r},\vec{k},t)\, c\,(1-\beta\cos\theta_i)\, dV d^3p\, d^3k\, dt, \tag{2.1.12}$$

where $\sigma_t(\vec{p},\vec{k})$ is the total cross section of Compton scattering, N_e and N_p are numbers of the electrons and photons, and $f_e(\vec{r},\vec{p},t)$ and $f_p(\vec{r},\vec{k},t)$ are the phase space intensity functions of the electrons and photons. Assuming that the electron bunch and laser pulse have Gaussian distributions in their phase spaces, the intensity functions can be separated into the spatial and momentum spaces: $f_e(\vec{r},\vec{p},t) = f_e(\vec{r},t)f_e(\vec{p})$ and $f_p(\vec{r},\vec{k},t) = f_p(\vec{r},t)f_p(\vec{k})$.

The total number of scattered photons can be obtained by integrating $dN(\vec{r},\vec{p},\vec{k},t)$ on entire phase space and time as follows:

$$\begin{aligned} N &= \int dN(\vec{r},\vec{p},\vec{k},t)\, dV d^3p\, d^3k\, dt \\ &= N_e N_p \mathcal{L}_s \int \sigma_t(\vec{p},\vec{k})\, f_e(\vec{p})\, f_p(\vec{k})\, d^3p\, d^3k, \end{aligned} \tag{2.1.13}$$

where

$$\mathcal{L}_s = c\,(1-\beta\cos\theta_i)\int f_e(\vec{r},t)\,f_p(\vec{r},t)\,dV dt \tag{2.1.14}$$

is the single-collision luminosity defined as the number of events produced per unit cross section of the scattering [25]. In the head-on collision case, $\theta_i = \pi$, with relativistic electrons of $\beta \sim 1$, that luminosity is rewritten as

$$\mathcal{L}_s = \frac{1}{2\pi}\left(\frac{\lambda z_R}{4\pi}+\beta_x\epsilon_x\right)^{-\frac{1}{2}}\left(\frac{\lambda z_R}{4\pi}+\beta_y\epsilon_y\right)^{-\frac{1}{2}}, \tag{2.1.15}$$

where λ is the laser wavelength, z_R is the Rayleigh range, $\beta_{x,y}$ are Twiss parameters of the electron beam, and $\epsilon_{x,y}$ are transverse emittance. As a conclusion, the total number of scattered photons in unit time is given by

$$\frac{dN}{dt} = fN_eN_p\mathcal{L}_s\overline{\sigma_t}, \tag{2.1.16}$$

where f is the repetition rate of the collision, $\overline{\sigma_t}$ is the averaged total cross section of Compton scattering; it can be approximated by σ_t when the energy spread of the electrons and laser photons are neglected. This expression shows that as the laser power increasing the flux of the scattered photon beam increases proportionally.

2.2 Principle of an optical resonant cavity

An optical resonant cavity is a device that realizes power storage of laser light; when the cavity resonates with incident laser light, the light accumulates coherently in the cavity. The power enhancement factor of the laser storage is expressed by the power reflectivity R of the cavity mirror: $1/(1-R)$. By constructing the cavity with high reflectivity mirrors, the large enhancement factor can be obtained, however, there is a problem that coherence collapses with slight phase change. In order to think about this problem, this section explains the principle of the optical resonant cavity. (For the spatial characteristics of the cavity, see Appendix A.)

2.2.1 Transmitted and reflected light of a Fabry-Pérot cavity

Figure 2.5 shows the most basic optical resonant cavity which consists of two concave mirrors (Fabry-Pérot cavity) [28]. When the input mirror (M1) of the cavity is irradiated with the incident laser light, a part of the light field goes through the mirror by the transmission coefficient t_1. The light in the cavity undergoes a change in amplitude by each round-trip with a factor of the reflection coefficient of cavity mirrors: r_1 and r_2. On the other hand, a part of the laser light inside the cavity exit from both the input (M1) and output (M2) cavity mirrors by each round-trip. Thus, the reflected light by the cavity is expressed by the superposition of the prompt reflection of the incident light and penetrations from the cavity, while the transmitted light is the superposition of the penetrations from the cavity.

The transmitted and reflected light fields (electric fields) $E_{tr}(t)$ and $E_{re}(t)$ are given by [29]

$$\begin{aligned}
E_{in}(t) &= E_0 e^{i\omega t}, && (2.2.1)\\
E_{tr}(t) &= E_0 e^{i\omega t}\left[t_1 t_2 e^{-i\omega\frac{l}{c}} + t_1 t_2 r_1 r_2 e^{-i\omega\frac{3l}{c}} + \cdots\right], && (2.2.2)\\
E_{re}(t) &= E_0 e^{i\omega t}\left[r_1 - r_2 t_1^2 e^{-i\omega\frac{2l}{c}} - r_1 r_2^2 t_1^2 e^{-i\omega\frac{4l}{c}} - \cdots\right], && (2.2.3)
\end{aligned}$$

where l is the cavity length (the distance between two mirrors), c is the speed of light, and $t_{1,2}$ are transmission coefficients of the cavity mirrors, respectively. The factor $e^{-i\omega\frac{2l}{c}}$ indicates the phase shift for each round-trip

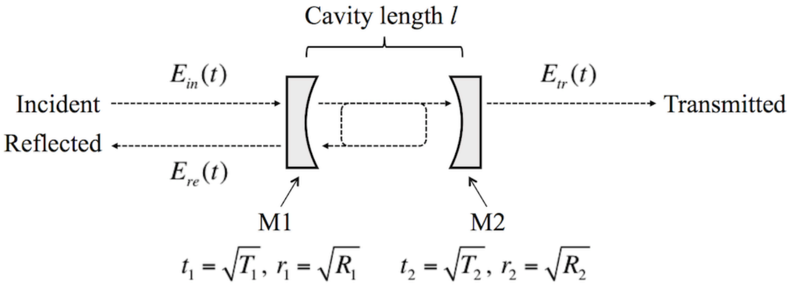

Figure 2.5: A conceptual drawing of a Fabry-Pérot cavity with the cavity length l. $r_{1,2}$ and $t_{1,2}$ are reflection and transmission coefficients, and $R_{1,2}$ and $T_{1,2}$ are intensity reflectivity and transmittance of the cavity mirrors.

of the light in the cavity. From infinite series of those equations, the transfer functions of the cavity are given by

$$\frac{E_{tr}}{E_{in}} = \frac{t_1 t_2 e^{-i\omega\frac{l}{c}}}{1 - r_1 r_2 e^{-2i\omega\frac{l}{c}}}, \tag{2.2.4}$$

$$\frac{E_{re}}{E_{in}} = \frac{r_1 - r_2(r_1^2 + t_1^2)e^{-2i\omega\frac{l}{c}}}{1 - r_1 r_2 e^{-2i\omega\frac{l}{c}}}. \tag{2.2.5}$$

For later use, another derivation method is shown in figure 2.6 [30, 31]. The transmitted field is derived by using the forward-going field $E_F(t)$ and the backward-going field $E_B(t)$; these fields are given by

$$E_F(t) = t_1 E_{in}(t) - r_1 E_B(t-T)e^{-i\omega T}, \tag{2.2.6}$$

$$E_B(t) = -r_2 E_F(t-T)e^{-i\omega T}, \tag{2.2.7}$$

where $T = 2l/c$ is the one round-trip time of the intra-cavity light. Substituting equation (2.2.7) to equation (2.2.6), the forward-going field is rewritten as

$$E_F(t) = t_1 E_{in}(t) + r_1 r_2 E_F(t-T)e^{-i\omega T}. \tag{2.2.8}$$

Assuming that the intra-cavity field settles down to the stead-state condition, we obtain the relation of $E_F(t) = E_F(t-T)$. Therefore, equation (2.2.8) can be solved as

$$E_F(t) = \frac{t_1}{1 - r_1 r_2 e^{-i\omega T}} E_{in}(t). \tag{2.2.9}$$

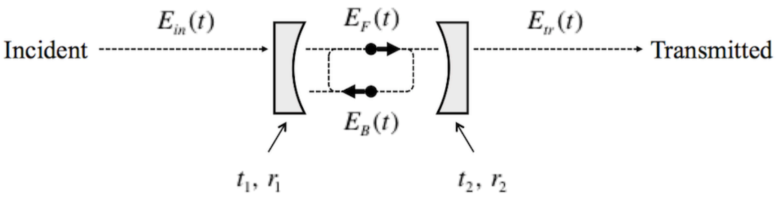

Figure 2.6: The conceptual drawing of the self-consistent scheme to introduce the transmitted light field from the cavity. $E_F(t)$ is the forward-going field and $E_B(t)$ the backward-going field.

By multiplying the transmission coefficient t_2, the transmitted field from the cavity is obtained as follows:

$$E_{tr}(t) = \frac{t_1 t_2 e^{-i\omega T/2}}{1 - r_1 r_2 e^{-i\omega T}} E_{in}(t). \tag{2.2.10}$$

2.2.2 Transfer functions of a Fabry-Pérot cavity and the cavity finesse

Assuming that two cavity mirrors have same intensity transmittance and reflectivity, $T_1 = T_2 = T$ and $R_1 = R_2 = R$, the transfer functions for the transmitted and reflected light intensities are given by

$$\frac{I_{tr}}{I_{in}} = \left|\frac{E_{tr}}{E_{in}}\right|^2 = \frac{T^2}{(1-R)^2 + 4R\sin^2\left(\omega/2\nu_{\mathrm{FSR}}\right)}, \tag{2.2.11}$$

$$\frac{I_{re}}{I_{in}} = \left|\frac{E_{re}}{E_{in}}\right|^2 = \frac{R\left[A^2 + 4(R+T)\sin^2\left(\omega/2\nu_{\mathrm{FSR}}\right)\right]}{(1-R)^2 + 4R\sin^2\left(\omega/2\nu_{\mathrm{FSR}}\right)}, \tag{2.2.12}$$

where R and T have the relations as follows:

$$R_i = r_i^2, \tag{2.2.13}$$

$$T_i = t_i^2; \tag{2.2.14}$$

A is the optical loss coefficient defined as

$$A = 1 - R - T; \tag{2.2.15}$$

ν_{FSR} is the free spectrum range of the cavity defined by

$$\nu_{\mathrm{FSR}} = \frac{c}{2l}. \tag{2.2.16}$$

From equation (2.2.11) and (2.2.12), it is found that the cavity resonates with the incident light under the resonant condition:

$$\frac{\omega}{2\nu_{\mathrm{FSR}}} = \frac{2\pi\nu}{2\nu_{\mathrm{FSR}}} = q\pi, \tag{2.2.17}$$

where ν is the optical frequency of the incident light, q is an integer called the mode number. The resonance condition can be also written as the relation of the wavelength λ and the cavity length l:

$$l = \frac{\lambda}{2} q. \tag{2.2.18}$$

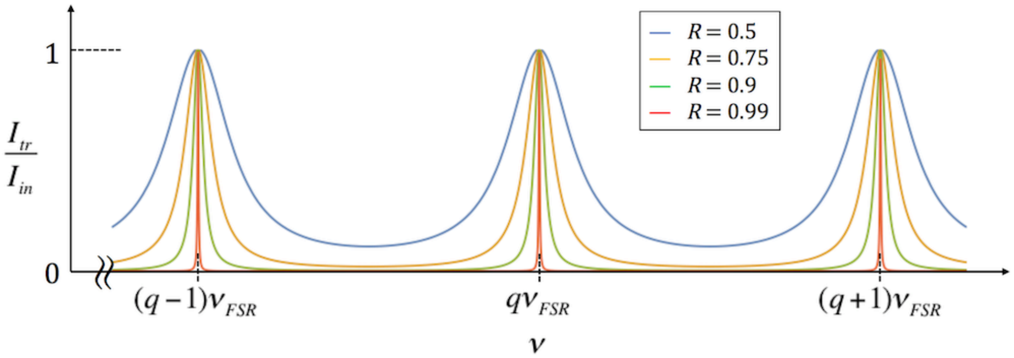

Figure 2.7: The transmitted light intensity with several reflectivities of the cavity mirrors. The transmitted intensity on the resonance condition equals the incident intensity in the case of without the optical loss on the mirrors.

Figure 2.7 and 2.8 show equation (2.2.11) and (2.2.12) as a function of ν with several R under the condition of $A = 0$. It is found that curves have resonance peaks (or dips) with a period of ν_{FSR} and the linewidth of the peak narrows as the reflectivity of the mirror approaches unity.

When the light frequency changes slightly by $\delta\nu$ around the resonance frequency, the denominator on the right side of equation (2.2.11) can be rewritten as

$$(1-R)^2 + 4R\sin^2\left(\frac{2\pi\delta\nu}{2\nu_{\rm FSR}}\right) \sim (1-R)^2 + 4R\left(\frac{\pi\delta\nu}{\nu_{\rm FSR}}\right)^2. \qquad (2.2.19)$$

From this relation, the full width at the half maximum (FWHM) of the resonant peak, $\Delta\nu$, can be calculated as follows:

$$\begin{aligned} (1-R)^2 + 4R\left(\frac{\pi}{\nu_{\rm FSR}}\frac{\Delta\nu}{2}\right)^2 &= 2(1-R)^2 \\ \left(\frac{\Delta\nu}{2}\right)^2 &= \frac{(1-R)^2}{4\pi^2 R}\nu_{\rm FSR}^2 \\ \Delta\nu &= \frac{1-R}{\pi\sqrt{R}}\nu_{\rm FSR}. \end{aligned} \qquad (2.2.20)$$

From this expression, the sharpness of the resonance peak can be defined as an important parameter of the cavity called finesse, which is also known as a guide of the resolution of an optical spectrum analyzer using a Fabry-Pérot

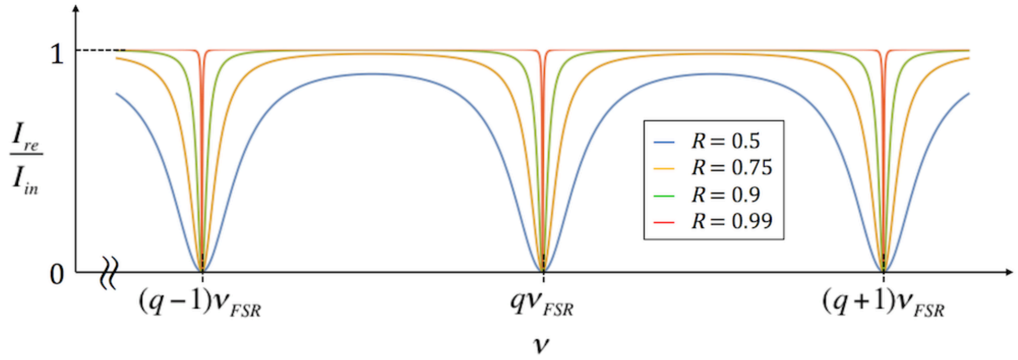

Figure 2.8: The reflected light intensity with several reflectivities of the cavity mirrors. The reflected intensity is zero on the resonance condition in the case of without the optical loss on the mirrors.

etalon. The finesse is given by

$$F = \frac{\nu_{\mathrm{FSR}}}{\Delta\nu} = \frac{\pi\sqrt{R}}{1-R} \sim \frac{\pi}{1-R}, \tag{2.2.21}$$

where the approximation is for the high reflectivity case ($R \sim 1$). For the case when the cavity length changes instead of the optical frequency, the FWHM of the length Δl can be defined as follows:

$$\begin{aligned} (1-R)^2 + 4R\left(\frac{2\delta l}{\lambda}\right)^2 &= 2(1-R)^2 \\ \delta l &= \frac{1-R}{\pi\sqrt{R}}\frac{\pi\lambda}{4}, \\ \therefore \Delta l = 2\delta l = \frac{\pi\lambda}{2F}. \end{aligned} \tag{2.2.22}$$

This expression shows the difficulty of maintaining the resonance condition; in order to maintain the resonance of the cavity, it is necessary to control the cavity length with an accuracy much smaller than the the length of $1/F$ of the light wavelength.

2.2.3 Power enhancement by an optical resonant cavity

The steady-state light intensities from the cavity under the resonance condition are shown in figure 2.9. When the optical loss A cannot be neglected, the transmitted intensity is smaller than the incident light and the reflected intensity does not become zero. The intra-cavity intensity I_{cav} is given by

$$I_{cav} = \frac{2T}{(1-R)^2} I_{in}, \tag{2.2.23}$$

where the indicated factor of 2 means that the light forms a standing wave in the cavity, and the coefficient $2T/(1-R)^2$ indicates the enhancement factor of the light power. In the case of $T = 1 - R$, the enhancement factor G will be proportional to the finesse or simply $1 - R$:

$$G = \frac{2T}{(1-R)^2} = \frac{2}{1-R} \sim \frac{2F}{\pi}. \tag{2.2.24}$$

It should be noted that the enhancement factor G is not only the power enhancement factor but also the factor for the interaction length of intra-cavity light.

2.2.4 Lifetime of the light inside the cavity

When the incident light is removed at $t = t_0$, the light power stored in the cavity decreases due to the transmission and the optical loss. In times $t > t_0$, the forward-going field in the cavity shown in equation (2.2.8) is given by

$$E_F(t + \frac{2l}{c}) = RE_F(t), \tag{2.2.25}$$

where we can neglect the exponential factor since the cavity had been resonated until the time $t < t_0$. With the Taylor series approximation, the

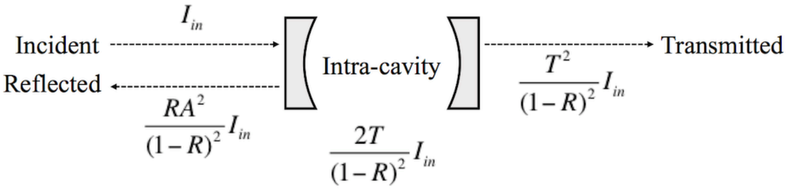

Figure 2.9: The steady-state intensities around the cavity at the resonance condition. The light power inside the cavity is enhanced by a magnitude of about the finesse.

left-hand side of equation (2.2.25) is rewritten as

$$E_F(t+\frac{2l}{c}) \sim E_F(t) + \frac{2l}{c}\frac{d}{dt}E_F(t). \tag{2.2.26}$$

Thus, the differential equation for the forward-going field is obtained:

$$\frac{d}{dt}E_F(t) = -\frac{c}{2l}(1-R)E_F(t). \tag{2.2.27}$$

The solutions of this differential equation and the forward-going intensity are calculated as follows:

$$\begin{aligned} E_F(t) &= E_F(t_0)\exp\left[-\frac{c}{2l}(1-R)(t-t_0)\right], & (2.2.28)\\ I_F(t) &= |E_F(t)|^2 = I_F(t_0)\exp\left[-\frac{(t-t_0)}{\tau_c}\right], & (2.2.29) \end{aligned}$$

where the decay time constant τ_c is given by

$$\tau_c = \frac{l}{c(1-R)} \sim \frac{l}{\pi c}F = \frac{1}{2\pi\Delta\nu}. \tag{2.2.30}$$

This decay time constant indicates the lifetime of the light inside the cavity and is the inverse of the resonance linewidth $\Delta\nu$. As will later be shown, measuring the lifetime of the intra-cavity light is an effective means for obtaining the cavity finesse.

2.3 Laser amplifier and oscillator

The principle of the feedback-free optical cavity is based on a ring laser oscillator; an optical resonant cavity is added as the storage cavity to the circulating optical path of the oscillator. In this experiment, we used an ytterbium-doped fiber amplifier (YDFA) which is known to operate as the almost four-level laser system [34]. In order to understand the transfer of energy between the amplifier, the laser cavity which is the circulating optical path and the storage cavity, the principle of a four-level laser system and the dynamic characteristics of laser oscillators are introduced in this section.

2.3.1 Four-level laser system

A four-level laser system consists of the ground level (0), the lower level of the laser transition (1), the upper level of the laser transition (2) and the excitation band (3) as shown in figure 2.10. Here, the atoms (doped ions of rare-earth metal in silica glass material) are excited from (0) to (3) by the light pumping process, and transition from (2) to (1) while coherently amplifying signal light. $N_i\,(i = 0, 1, 2, 3)$ are occupation numbers or population of the atoms [number/m^3] at each level. The population inversion associated with laser transition can be denoted as $N_2 - N_1$. In the ideal four-level system, since the transition from (1) to (0) and the transition from (3) to (2) are very fast transitions, we can neglect those population: $N_1 = N_3 = 0$. Furthermore, the population inversion can be rewritten as $N_2 - N_1 = N_2$.

In order to describe transitions of the atoms each level, we use the stimulated transition rate $W(\nu)$ [1/s] and the spontaneous emission transition rate γ_2 [1/s], where ν is optical frequency and γ_2 is the inverse of the fluorescence lifetime τ_2 of the level (2):

$$\gamma_2 = \frac{1}{\tau_2}. \tag{2.3.1}$$

The time variation of the population inversion which is known as the rate equation is given by [32]

$$\frac{dN_2}{dt} = (N_t - N_2)W_p(\nu_p) - \gamma_2 N_2 - N_2 W_s(\nu_s), \tag{2.3.2}$$

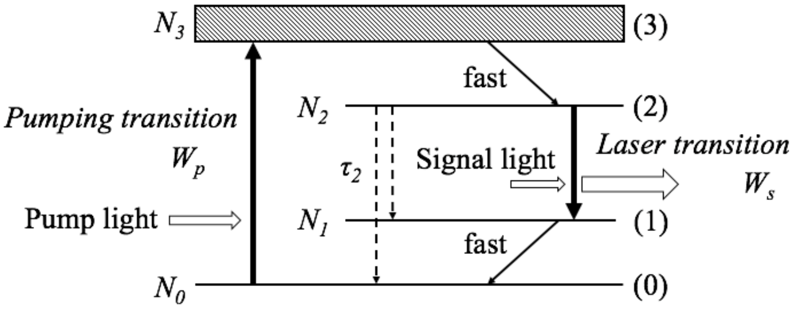

Figure 2.10: An energy level diagram of a four-level system. Details are in the main text.

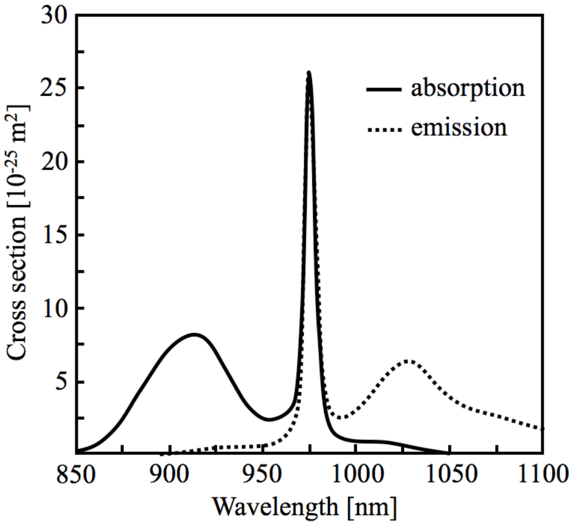

Figure 2.11: Absorption and emission cross sections of a ytterbium-doped optical fiber. The data is from [34].

where the subscripts p, s indicate the pump light and signal light that we want to amplify; each term are corresponding to the pumping, spontaneous emission and stimulated emission process in order from the left, respectively. The transition rate of the pumping process is proportional to the ground level populatio, $N_0\,(= N_t - N_2)$, where N_t is the total number of atoms in the unit volume.

The stimulated transition rate $W(\nu)$ are expressed as follows:

$$W(\nu) = \frac{\sigma_{em(ab)}}{h\nu}\Gamma I, \tag{2.3.3}$$

where $\sigma_{em(ab)}$ is the stimulated emission (or absorption) cross section [m^2]; I is the light intensity [W/m^2]; Γ is the spatial overlapping coefficient between the light and the laser medium; $h\nu$ is the photon energy [J], where h is Plank's constant. Using this expression, the rate equation is rewritten as

$$\frac{dN_2}{dt} = (N_t - N_2)\frac{\sigma_{ab}}{h\nu_p}\Gamma_p I_p - \gamma_2 N_2 - N_2\frac{\sigma_{em}}{h\nu_s}\Gamma_s I_s. \tag{2.3.4}$$

For accurate analysis, the rate terms should be integrated over a range of optical frequencies from zero to infinity since the pump and signal lights have the finite linewidth. Furthermore, the absorption and emission cross sections of a ytterbium-doped optical fiber, figure 2.11, shows that both spectra overlap in wide wavelength range; in many cases, the wavelength of the pump light is chosen at 915 nm or 976 nm; the amplifiable wavelength band of the YDFA is in the range of 1020 nm to 1070 nm because the emission cross section is larger than the absorption cross section in that range. The rate equation can be modified as follows [33]:

$$\frac{dN_2}{dt} = \int_0^\infty \frac{I(\nu)}{h\nu}\Gamma\left[(N_t - N_2)\sigma_{ab} - N_2\sigma_{em}\right]d\nu - \gamma_2 N_2. \tag{2.3.5}$$

It is not necessary to use this equation when the pump and signal lights are approximated to monochromatic. Analysis of the amplified spontaneous emission (ASE) in fiber amplifiers, for example, require such a detailed expression.

2.3.2 Equations of the light propagation

The light power generated per unit volume [W/m^3] by the stimulated emission process is given by

$$N_2 W_s(\nu_s) \times h\nu_s = N_2\sigma_{em}\Gamma_s I_s. \tag{2.3.6}$$

This additional optical power is coherent to the incident signal light, so the intensity of the signal is amplified along the propagation direction z according to the following differential equation:

$$\frac{dI_s}{dz} = \Gamma_s N_2 \sigma_{em} I_s. \tag{2.3.7}$$

Similarly, we obtain the following differential equation for the absorption process of the pump light:

$$\frac{dI_p}{dz} = \Gamma_p (N_t - N_2)\sigma_{ab} I_p. \tag{2.3.8}$$

In the case of a fiber amplifier, there are two directions of light propagation. Consider the traveling direction of the signal light is taken as the forward direction, the differential equations for the two propagation directions of the pump light are given by

$$\pm\frac{dI_p^\pm}{dz} = \Gamma_p (N_t - N_2)\sigma_{ab} I_p^\pm, \tag{2.3.9}$$

where superscripts + and − indicate the forward and backward directions, respectively. In generally, there are three schemes of the optical pumping for fiber amplifiers: the forward pumping, backward pumping and the double-side pumping. This two-directions analysis is also essential for analysis of the ASE [33].

2.3.3 Steady-state behavior of a laser oscillator

Consider a laser oscillator consisting of an amplifier and a laser cavity which is an arbitrary optical feedback path. For simplicity, the rate equation (2.3.4) is rewritten as

$$\frac{dN_2}{dt} = R_p - \gamma_2 N_2 - K N_2 q, \tag{2.3.10}$$

where

$$R_p = N_t \frac{\sigma_{ab}}{h\nu_p} \Gamma_p I_p, \tag{2.3.11}$$

$$K = \sigma_{em} \Gamma_s, \tag{2.3.12}$$

and

$$q = \frac{I_s}{h\nu_s} \tag{2.3.13}$$

is the photon number density [number/m^2]. The pumping term is replaced by the constant R_p assuming that the steady state population inversion is much smaller than the ground level population: $N_t - N_2 \sim N_t$. The rate equation for the photon number is given by

$$\frac{dq}{dt} = K N_2 q - \gamma_L q, \tag{2.3.14}$$

where γ_L is the photon decay rate of the laser cavity; it defined by optical loss and the traveling time in the cavity:

$$\gamma_L = \frac{-\ln \alpha_{\mathrm{loop}}}{\tau_L}, \tag{2.3.15}$$

where α_{loop} is the optical loss in one round-trip pass in the laser cavity, and τ_L is the decay time constant of the laser cavity.

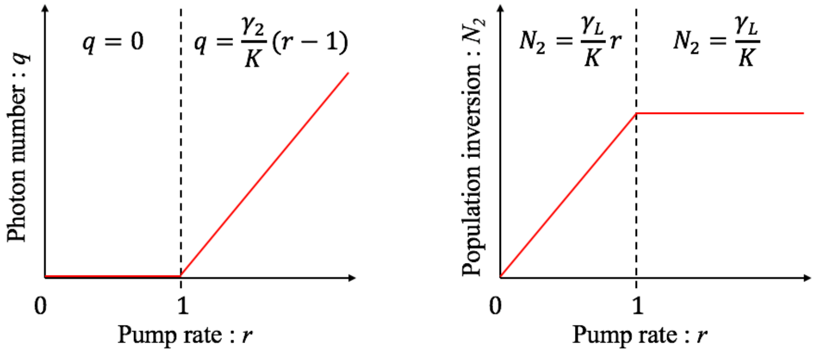

Figure 2.12: The steady state behavior of a laser oscillator. $r = 1$ is the threshold of the laser oscillation. Details are in the main text

The threshold condition of the laser oscillation is obtained by calculating the steady-state population inversion N_2^{ss} and the photon number q^{ss}. From equation (2.3.10), the steady-state condition is

$$\begin{aligned} 0 &= R_p - \gamma_2 N_2 - K N_2 q, \\ \therefore N_2^{ss} &= \frac{R_p}{\gamma_2 + K q^{ss}}. \end{aligned} \tag{2.3.16}$$

From equation (2.3.14), the steady-state condition is also

$$\begin{aligned} 0 &= K N_2^{ss} q^{ss} - \gamma_L q^{ss} \\ &= (K N_2^{ss} - \gamma_L) q^{ss}, \end{aligned}$$

$$\therefore \begin{cases} q^{ss} = 0 \\ N_2^{ss} = \gamma_L / K \end{cases}. \tag{2.3.17}$$

Substituting the solution of N_2^{ss} for equation (2.3.16), another solution of the steady state photon number is obtained as

$$q^{ss} = \frac{R_p}{\gamma_L} - \frac{\gamma_2}{K}. \tag{2.3.18}$$

Taking into account the solution $q^{ss} = 0$, the threshold pumping rate for laser oscillation, R_p^{th}, is obtained as

$$R_p^{th} = \frac{\gamma_2 \gamma_L}{K}. \tag{2.3.19}$$

With this threshold pumping rate, we defined the pump ratio r as follows:

$$r \equiv \frac{R_p}{R_p^{th}} = \frac{K}{\gamma_2 \gamma_L} R_p. \tag{2.3.20}$$

The steady state behavior is distinguished into two situations at the threshold $r = 1$ as shown in figure 2.12. When $r < 0$, the population inversion increases in proportion to the pump rate and the laser oscillation does not build up ($q^{ss} = 0$). When $r > 0$, the population inversion is saturated at $N_2^{ss} = \gamma_L / K$ and the number of laser photons simply increases in proportion to the pump rate.

2.3.4 Relaxation oscillations

When the laser oscillation is perturbed from its steady state, spiking and damped oscillations occur. Such behavior is well known as relaxation oscillations [35] and described by two differential equations of the population inversion equation (2.3.10) and the photon number equation (2.3.14). Those equations, however, can not be analytically solved due to the coupled term of KN_2q. Thus, we carry out a linearized analysis and introduce simple analytic solutions for relaxation oscillations.

Let's consider small perturbations of N_2 and q from their steady state values as follows:

$$N_2 = N_2^{ss} + \Delta N, \tag{2.3.21}$$

$$q = q^{ss} + \Delta q, \tag{2.3.22}$$

where $\Delta N \ll N_2^{ss}$ and $\Delta q \ll q^{ss}$. Substituting these in equations (2.3.10) and (2.3.14), and neglecting the coupling term $\Delta N \Delta q$, the following equations for ΔN and Δq are obtained:

$$\begin{aligned}
\frac{d\Delta N}{dt} &= R_p - \gamma_2(N_2^{ss} + \Delta N) - K(N_2^{ss} + \Delta N)(q^{ss} + \Delta q) \\
&= R_p - \gamma_2 N_2^{ss} - K N_2^{ss} q^{ss} - \gamma_2 \Delta N - K N_2^{ss} \Delta q - K q^{ss} \Delta N \\
&\quad -K \Delta N \Delta q \\
&= -\gamma_2 \Delta N - K N_2^{ss} \Delta q - K q^{ss} \Delta N \\
&= -\gamma_2 \Delta N - \gamma_L \Delta q - (r-1)\gamma_2 \Delta N \\
&= -\gamma_L \Delta q - r\gamma_2 \Delta N, \qquad (2.3.23) \\
\frac{d\Delta q}{dt} &= K(N_2^{ss} + \Delta N)(q^{ss} + \Delta q) - \gamma_L(q^{ss} + \Delta q) \\
&= K N_2^{ss} q^{ss} - \gamma_L q^{ss} + K N_2^{ss} \Delta q + K q^{ss} \Delta N - \gamma_L \Delta q + K \Delta N \Delta q \\
&= -\gamma_2 \Delta N + K N_2^{ss} \Delta q - K q^{ss} \Delta N \\
&= \gamma_L \Delta q + (r-1)\gamma_2 \Delta N - \gamma_L \Delta q \\
&= (r-1)\gamma_2 \Delta N, \qquad (2.3.24)
\end{aligned}$$

where relations $N_2^{ss} = \gamma_L/K$ and $q^{ss} = (r-1)\gamma_2/K$ are used. By differentiating equation (2.3.24) with respect to time, and using equation (2.3.23) to eliminate ΔN from the resulting equation, the linearized equation for Δq is obtained as

$$\frac{d^2\Delta q}{dt^2} + r\gamma_2 \frac{d\Delta q}{dt} + (r-1)\gamma_2\gamma_L \Delta q = 0. \qquad (2.3.25)$$

The equation (2.3.25) is the second-order system with the natural angular frequency ω_n and the damping ratio ζ given by

$$\omega_n = \sqrt{(r-1)\gamma_2\gamma_L}, \qquad (2.3.26)$$

$$\zeta = \frac{r\gamma_2}{2\omega_n} = \frac{r}{2\sqrt{r-1}} \left(\frac{\gamma_2}{\gamma_L}\right)^{\frac{1}{2}}. \qquad (2.3.27)$$

When the steady state light intensity is perturbed, the exponentially damped oscillations occur with the angular frequency of

$$\omega_{ro} = \omega_n \sqrt{1-\zeta^2} \qquad (2.3.28)$$

and the decay time constant of

$$\tau_{ro} = \frac{2}{r\gamma_2}. \qquad (2.3.29)$$

The behavior of relaxation oscillations depends on the relative size of the decay rates γ_2 and γ_L. In most gas lasers, its atomic fluorescence lifetime is short and the cavity decay time constant is relatively long due to its long cavity length; γ_2 and γ_L are of same order of magnitude: $\gamma_2 \sim \gamma_L$. Since the damping ratio ζ is almost unity, the laser intensity behaves non-spiking relaxation oscillations. On the other hand, most semiconductor lasers and many solid-state lasers indicate the very much slower atomic decay rate compared to the cavity decay rate: $\gamma_2 \ll \gamma_L$. Such lasers show the strong spiking on relaxation oscillations owing to their small damping ratio. The time period of the spiking T_{ro} is given by $T_{ro} = 2\pi/\omega_{ro}$ or $T_{ro} = 2\pi/\omega_n$ because ζ^2 term in equation (2.3.28) can be neglect.

Chapter 3

Ultra-low loss mirrors and finesse measurement techniques

3.1 Ultra-low loss mirrors

One of the most fundamental ploblems to develop a high finesse optical resonant cavity is the gaining quality of the cavity mirrors. An optical mirror is characterized by three parameters which satisfy the relation (2.2.15): the intensity reflectance R, transmittance T and loss coefficient A. The reflectance and transmittance are determined by a design of the reflection coating on a substrate of the mirror. The intensity loss is caused by the scattering and absorption on the surface of the coat and substrate. The achieving loss is limited by the manufacturing accuracy of the mirror; only a few companies can produce an ultra-low loss mirror with less than ppm ($= 10^{-6}$) loss coefficient [36].

Since the surface condition of such high quality mirror can easily get deteriorated by contamination, one must handle it carefully. Additional loss decreases the cavity finesse, and the absorption loss will be become a problems in the application of high power lasers because of thermal deformation of the mirror. Thus, studies on handling method of ultra-low loss mirrors are also important in the development of high finesse cavity systems.

Ultra-low loss mirrors are manufactured by the dielectric multilayer coating, which is formed by depositing high refractive index material and low refractive index material on a glass substrate alternately. The ion-beam sputtering process is widely applied to form the multilayer coating since it can make dense coats with low roughness; the scattering loss of an optical mirror mainly depends on the roughness of the glass substrate. The surface roughness is characterized by the total integrated scattering (TIS) which is related to the root-mean-square of the roughness δ [37]:

$$\mathrm{TIS} = \left(\frac{4\pi\delta}{\lambda}\right)^2 . \tag{3.1.1}$$

This equation indicates that the angstrom roughness is required to realize the ppm-order scattering loss with visible to near-infrared wavelength range.

3.2 Scattering loss measurement and handling of the mirror

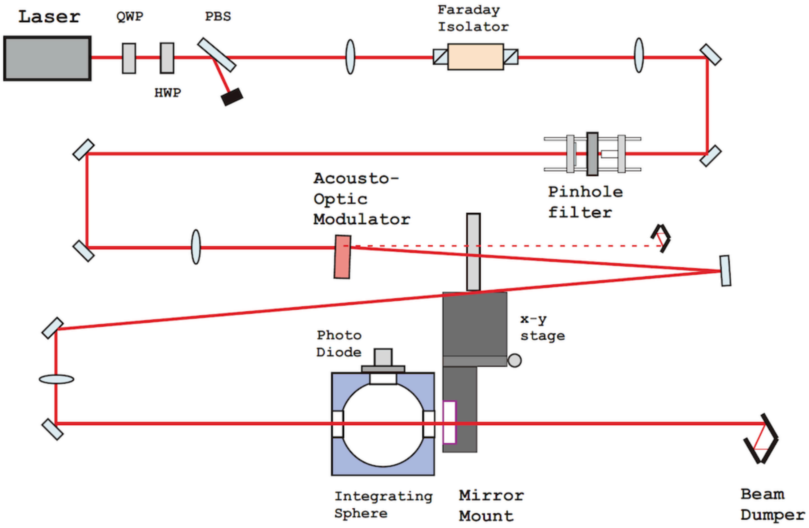

Figure 3.1: The optical setup of the scatter meter at TAMA experimental hall in National Astronomical Observatory of Japan (NAOJ) [37]. It can measure the 2-dimensional map of the TIS on a mirror surface.

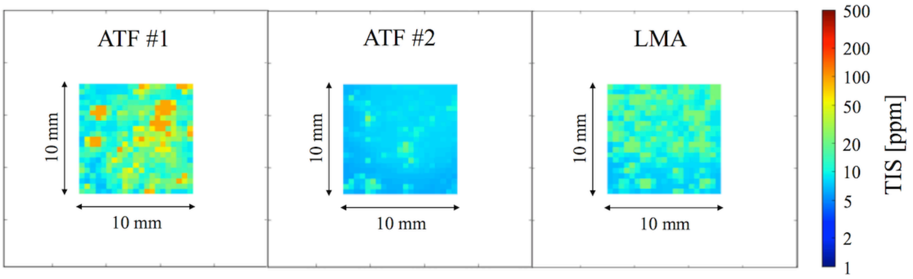

Figure 3.2: Measurement results of the scattering losses of our ultra-low loss mirrors. Those values had systematic errors of a few ppm.

In order to evaluate the performance of our low loss mirrors, we measured the scattering loss of those by using the scatter meter in National Astronomical Observatory of Japan (NAOJ) [37]. The optical setup of the measurement is shown in figure 3.1. The incident laser light was shaped in the fundamental Gaussian mode by a pinhole filter and flushed on the measured mirror surface. While the laser irradiated on the flat surface area of the mirror was reflected back to the incident trajectory, scattered light at the rough mirror surface was lead to a photo-diode detector by the integrated sphere. The scattered light intensity was measured by scanning the position of the mirror by a x-y stage. Here, the incident laser was switched on/off by an acousto-optic modulator with the intensity modulation of 1 MHz in order to improve the signal-to-noise ratio.

The ultra-low loss mirrors were flat mirrors with the diameter of 25.4 mm. Those mirrors were provided from two suppliers; one of them was Laboratoire Materiaux Avances (LMA, France) and their mirrors had the reflectivity of about 99.999 % according to the specification; another supplier was Advanced Thin Films (ATF, USA) and their mirrors had the loss coefficient of as low as 1 ppm according to the specification. Figure 3.2 shows measurement results of the scattering losses at the central area of 1 cm^2 on each mirror surface, where mirrors were referred as ATF#1, ATF#2 and LMA. The obtained averaged scattering losses were 25.0 ppm, 8.1 ppm and 12.9 ppm for ATF#1, ATF#2 and LMA, respectively, where value uncertainty was a few ppm. We found that the mirror labeled ATF#1 had practically large scattering losses and that value was far from its specifica-

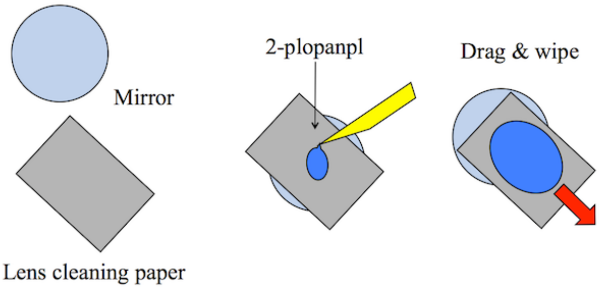

Figure 3.3: A schematic drawing of the drag-wiping technique. The detail is described in the main text or [38].

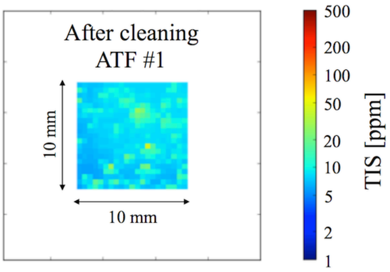

Figure 3.4: Measured scattering losses after the cleaning by the drag-wiping technique. The scattering losses of other mirrors were also improved by cleaning the mirror surfaces.

tion value.

In order to clean the contaminated mirror, ATF#1, we applied the drag-wiping technique [38]. Figure 3.3 shows a schematic drawing of that method. A cleaning paper is put on the mirror surface and a drop of pure 2-plopanol is applied on it. And then, the surface is wiped by dragging out lens-cleaning papers. Figure 3.4 shows the scattering losses of ATF#1 after the cleaning. The averaged scattering loss was improved from 25.0 ppm to 9.2 ppm with the minimum value of 4 ppm. Finally, all averaged scattering losses were successfully improved from the values before the cleaning to less than 10 ppm.

3.3 Finesse measurement techniques

There are several techniques to measure the cavity finesse depending on the magnitude of the finesse. According to equation (2.2.21), the finesse measurement means the measurement of the effective reflectivity of the cavity mirrors. In this section, some typical methods are introduced.

3.3.1 Cavity ring-down technique

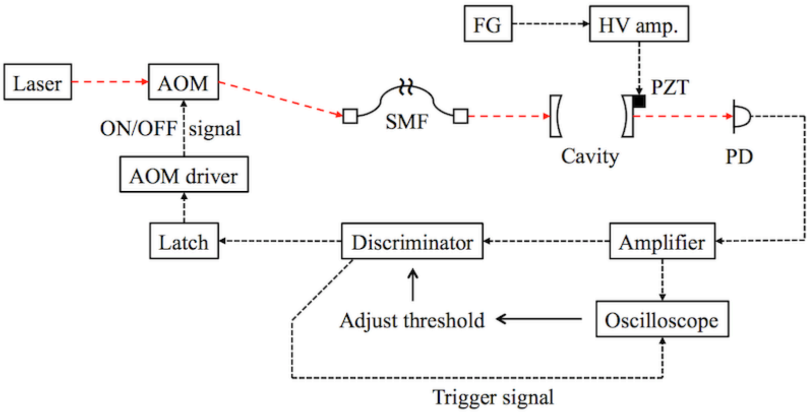

Figure 3.5: A schematic diagram of the cavity ring-down technique. AOM: acousto-optic modulator, SMF: single mode fiber, FG: function generator, HV amp.: high-voltage amplifier, PZT: piezo electric transducer, PD: photo-diode.

The time decay of the light in a Fabry-Pérot cavity is given by equation (2.2.29). Since the decay time constant is related to the cavity finesse and the cavity length as shown in equation (2.2.30), the finesse can be obtained by observing the time decay of the transmitted light from the cavity; this method is called cavity ring-down technique.

A schematic diagram of the cavity ring-down technique is shown in figure 3.5. At the first, the optical cavity had been aligned with the fundamental Gaussian mode of the incident laser light. The transmitted light from the cavity was monitored while scanning the cavity length with a piezo-electric transducer (PZT) actuator. When the cavity and the incident light closed

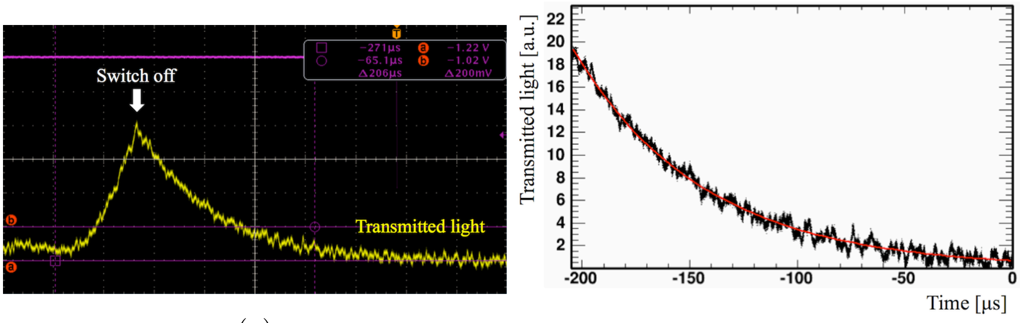

(a)

(b)

Figure 3.6: (a) Observed time decay signal (cavity ring-down signal) by using an oscilloscope. (b) The result of fitting with an exponential fit function.

to the resonant condition, increase of the transmitted light power was observed. Then, the incident light was shut-off by an acousto-optic modulator (AOM) when the light power reached the certain threshold level.

The obtained data of the time decay signal, which is called as ring-down signal, was fitted by an exponential function. An example of the measurement results for the cavity consisting of ultra-low loss mirrors provided by LMA is shown in figure 3.6a. The cavity length l was 0.216 ± 0.002 m and the fall time of AOM was less than 4 μs. By fitting the data with an exponential function as shown in figure 3.6b, the decay time constant τ_c, finesse F and the corresponding effective reflectivity R were obtained as $\tau_c = 60.21 \pm 0.03$ μs, $F = 263,000 \pm 2,000$ and $R = 99.99880 \pm 0.00001$ %, respectively.

3.3.2 Sideband technique

When the magnitude of the cavity finesse is relatively low, the cavity ring-down technique cannot be applied since the decay time constant is too short to measure precisely. On the other hand, the cavity linewidth which is inverse of the decay time becomes larger, thus the frequency-domain-measurement technique known as sideband technique can be used. In this method, frequency modulation is applied to the incident light to make side-

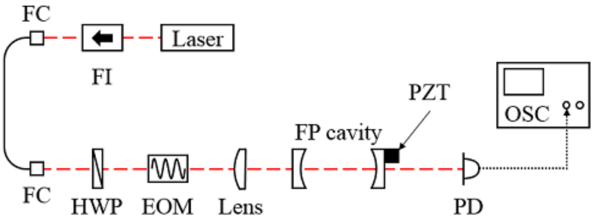

Figure 3.7: The setup diagram of the finesse measurement by the sideband method. FI: Faraday isolator, FC: fiber coupler/collimator, HWP: half wave plate, EOM: electro-optical modulator, PZT: piezo-electro transducer, PD: photo detector, OSC: oscilloscope.

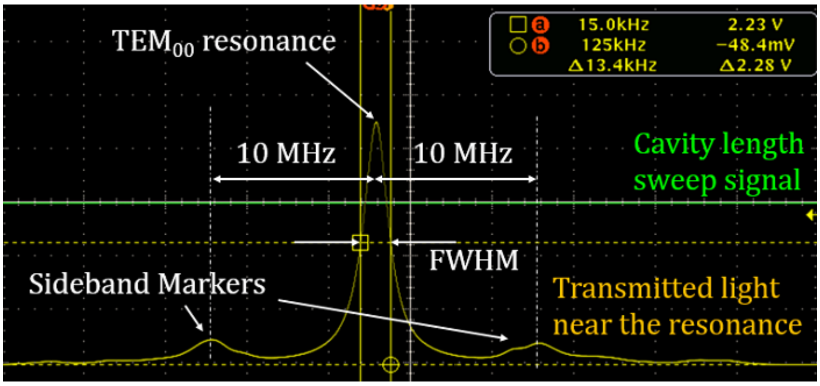

Figure 3.8: Measured resonance signal of the transmitted light. Small resonance signals at around the highest peak indicate the sideband lights.

band compornents as a frequency marker. Since the modulation frequency can be well controlled, the linewidth is measured with good measurement accuracy.

The setup diagram of the sideband method is shown in figure 3.7. FI is a Faraday isolator, two FCs are single mode fiber collimator/coupler, HWP is a half-wave plate, EOM is an electro-acoustic modulator, and PD is a photo-diode detector, respectively. The cavity length l and the free spectral range ν_{FSR} were 0.216 ± 0.002 m and 694.4 ± 6.4 MHz, respectively. The expected finesse and linewidth were $O(100)$ and $O(1)$ MHz due to the mirror reflectivity of 99.5 %, which is from the specification. The fundamental Gaussian mode of the incident light was well aligned to the cavity by using matching lens. And EOM gave 10 MHz sideband frequency to the incident light.

Figure 3.8 shows the observed temporal signal of the transmitted light. Since the cavity length was changed linear by using the PZT actuator, an Airy function shape appeared as the resonance peak (refer figure 2.7). This resonant peak was composed of the light with the carrier frequency which was the original optical frequency of the incident laser. Since the laser was modulated by EOM, the sidebands were observed at both sides of the resonance of the carrier light. Here, the observed time distance between the sideband and carrier peaks correspond to the modulation frequency of 10 MHz. As a result, the cavity linewidth $\Delta\nu$, finesse F and effective reflectivity R were obtained as $\Delta\nu = 1.85$ MHz, $R = 375 \pm 17$ and $R = 99.16 \pm 0.04$ %, respectively. The errors were mainly from the uncertainty of the cavity length.

3.3.3 Frequency response function technique

The linewidth of the resonance peak can be evaluated by measuring the cavity's response function which means the frequency response around its resonance frequency [39]. Figure 3.9 shows a conceptual scheme of this method. By applying amplitude modulation to the incident laser with the frequency Ω while the cavity is resonated at ω_0, the frequency components of ω_0, $\omega_0 - \Omega$ and $\omega_0 - \Omega$ show up. The carrier light with the frequency ω_0 passes through the cavity without any optical loss while the sidebands are attenuated since those are off resonance with the phase difference of Ω.

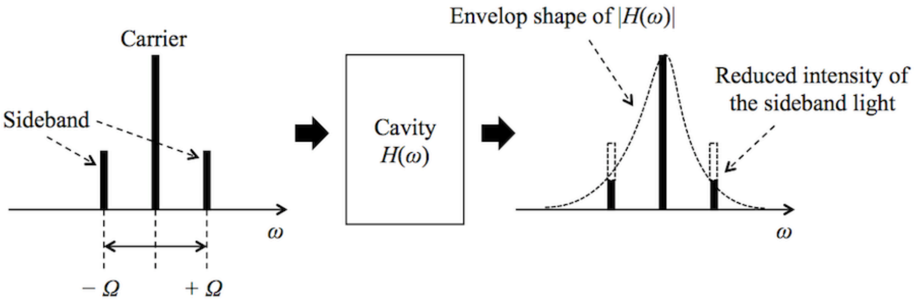

Figure 3.9: A conceptual scheme of the frequency response function technique with intensity modulation. The detail is described in [39]

According to the reference [39], in the case of $\Omega/\nu_{\mathrm{FSR}} \ll 1$, the transfer function for the sideband is given by

$$H^{\mathrm{IM}}(\Omega) = \left(\frac{T}{1-R}\right)^2 \frac{1}{1+i(2\Omega/\Delta\omega)}, \tag{3.3.1}$$

where $\Delta\omega$ is a linewidth of the cavity in FWHM. From equation (3.3.1), the gain and the phase delay are written as

$$|H^{\mathrm{IM}}(\Omega)| = \left(\frac{T}{1-R}\right)^2 \frac{1}{\sqrt{1+(2\Omega/\Delta\omega)^2}}, \tag{3.3.2}$$

$$\arg[H^{\mathrm{IM}}(\Omega)] = \tan^{-1}(2\Omega/\Delta\omega). \tag{3.3.3}$$

The cavity behaves as a first-order low pass filter for the small frequency Ω. We can obtain the linewidth by measuring the intensity of the sidebands as a function of Ω; the finesse can be obtained from equation (2.2.21) with the free spectral range of the cavity. The advantage of this technique is that finesse can be measured while keeping the cavity on resonance.

Chapter 4

Development of a high finesse feedback-free optical cavity

The development of a feedback-free optical cavity was carried out with two steps of strategy. Firstly, the feedback-free cavity with low finesse cavity was constructed to verify the self-resonating mechanism. Secondly, an optical cavity with high finesse and narrow linewidth was constructed and its operation was demonstrated.

4.1 Laser storage with a low finesse optical cavity

4.1.1 Construction of a feedback-free optical cavity

At the first, we constructed a feedback-free optical cavity with relatively low finesse. The optical setup of the feedback-free cavity is shown in figure 4.1. An optical amplifier consisted of a ytterbium-doped single mode fiber (YDF) with the mode field of 4.4 μm in diameter and 38 cm long. The amplifier was excited by a forward pumping light delivered from a stabilized laser diode (LD) via a wavelength division multiplexer coupler (WDM). The central wavelength of the pump laser was 976 nm and its maximum power was 330 mW. Here the amplifier had a wide gain bandwidth of about 50 nm with the gain maximum at 1034 nm. A polarization-independent Faraday

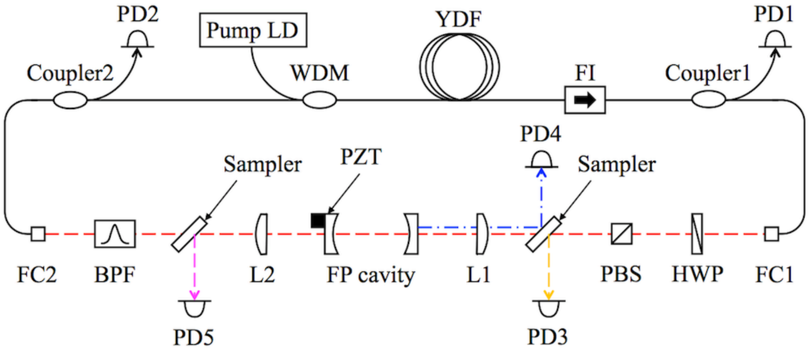

Figure 4.1: A schematic diagram of the feedback-free cavity with the low finesse cavity. The detail is in the main text.

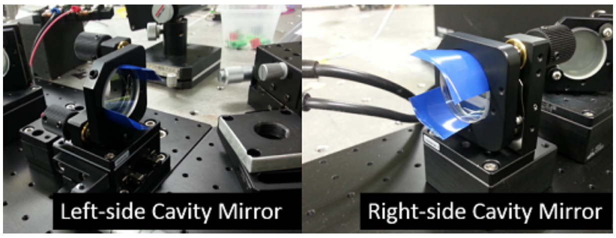

Figure 4.2: A photograph of the low finesse cavity. Two cavity mirrors mounted on kinematic mirror holders. The left-side holder has a PZT actuator.

isolator (FI) was inserted to determine the direction of propagation of the laser light. Two fused couplers with the brunching ratio of 99:1 (Coupler1, 2) were inserted to measure the laser power using photo-diode detectors (PD1, 2). Optical fibers used in this system were single mode fiber and both ends were connected to the free-space via collimator/couplers (FC1, 2). A polarizing beamsplitter (PBS) made linear polarization in the free-space. A half-wave plate (HWP) was placed to correct the direction of the polarization. The power of the laser light in the cavity was monitored with detectors (PD3, 4, 5) by sampling a part of light using pellicle mirrors. The optical cavity consisted of concave mirrors which had the effective reflectivity of $R = 99.16 \pm 0.04$ % and kinematic mirror holders as shown in figure 4.2. The free spectral range and the finesse were $\nu_{FSR} = 694.4 \pm 6.4$ MHz and $F = 375 \pm 17$, respectively. The cavity was mode-matched to a fundamental mode of from/to the optical fibers by matching lens (L1, 2) with the coupling efficiency of more than 90 %. An etalon type band pass filter (BPF) of typical center wavelength of 1064 nm was inserted for selecting the oscillation wavelength. Its center wavelength was able to be adjustable by tilting the BPF. All of experimental components was constructed on a vibration removal board in the air. The room temperature was maintained at 23.8 ± 0.5 °C during the experiment.

4.1.2 Laser oscillation and its behavior

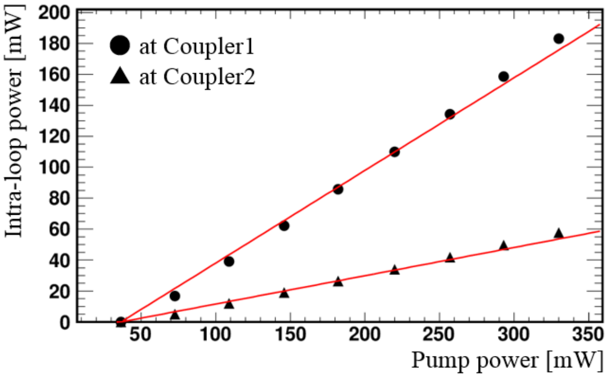

Figure 4.3: The measured laser light power as a function of the pump power. The feedback-free cavity was laser oscillated with the threshold pump power of about 45 mW.

Figure 4.3 shows the light power P_{loop} measured at Coupler1 and Coupler2 as a function of the pump power P_p applied by the laser diode, where the measured power was corrected by the brunching ratio of samplers. We observed continuous laser oscillation with a certain threshold of the pump power P_{th}. The data fitted with a linear function of

$$P_{loop} = \eta_s(P_p - P_{th}), \tag{4.1.1}$$

where η_s is the slope efficiency. The obtained parameters were

$$\eta_s^{\mathrm{C1}} = 0.599 \pm 0.001, \qquad P_{th}^{\mathrm{C1}} = 45 \pm 2 \text{ mW},$$
$$\eta_s^{\mathrm{C2}} = 0.183 \pm 0.001, \qquad P_{th}^{\mathrm{C2}} = 46 \pm 3 \text{ mW},$$

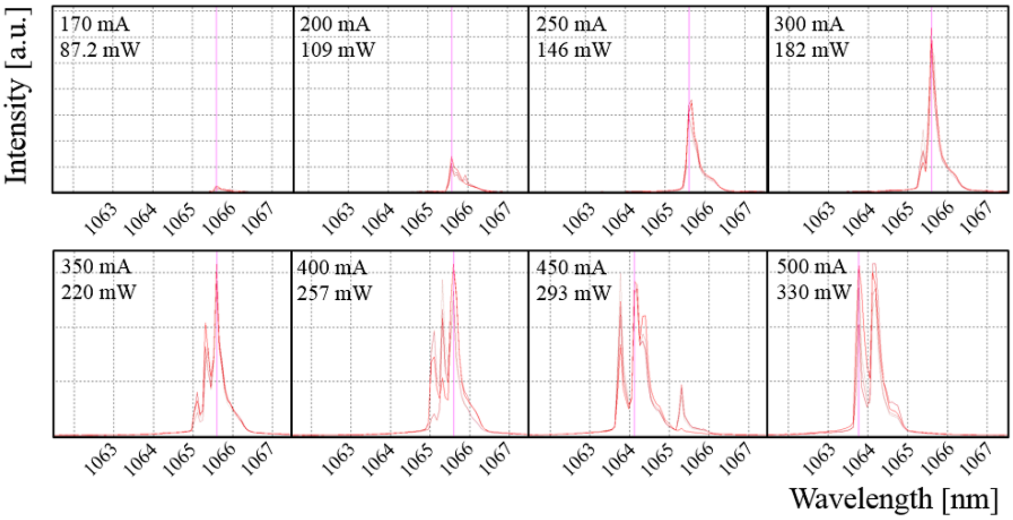

Figure 4.4: Measured laser spectra with several pump power conditions. The lasing wavelength was mainly defined by the band pass filter having the center wavelength of about 1064 nm.

where indices of C1, C2 mean measured points of Coupler1 or Coupler2. Since $\eta_s^{\mathrm{C2}}/\eta_s^{\mathrm{C1}} = -5.1$ dB and the optical loss of the isolator (FI) was typically 1.3 dB, the total optical losses except for the loss in YDF was estimated as 6.4 dB.

Figure 4.4 shows laser spectra measured at Coupler1 by a spectrometer (HR 2000+, Ocean Optics, Inc.) with the spectrum resolution of about 0.1 nm in FWHM. What shown at the upper-left of each pictures is the driving current to LD and the corresponding pump power. The central wavelength of the laser light was stable at 1066 nm up to the pump power of 182 mW, and it shifted to lower wavelength of around 1064 nm by increasing the pump power. At the pump power more than 200 mW, the lasing wavelength was mode-hopping frequently with a variation range of about 1 nm.

4.1.3 Relaxation oscillations

Figure 4.5a shows a typical time variation of the laser intensity measured at the PD2. The spiking and the damping oscillation were observed. Figure 4.5b shows power spectra of the light intensity measured by a FFT (Fast

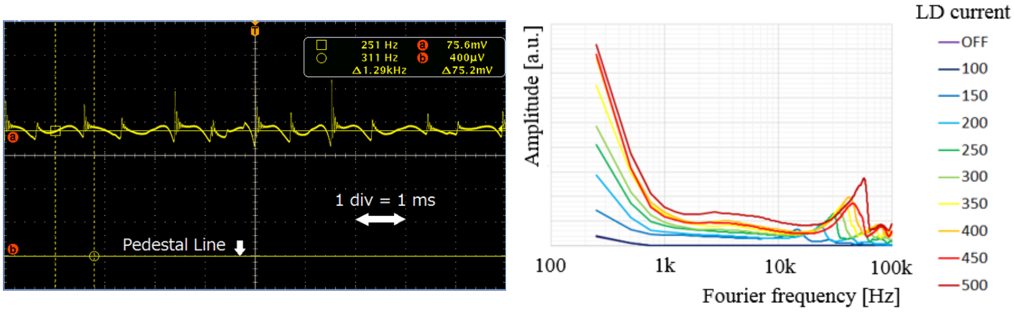

(a)

(b)

Figure 4.5: (a) A typical time response of the laser intensity measured at PD2. There were spiking intensity changes with damping oscillations. (b) Measured power spectra of the intensity by FFT analyzer. Each peak indicated the frequency of relaxation oscillations.

Fourier Transform) analyzer. Each colored line corresponds to different conditions of the pump power. Peaks at tens of kHz are corresponded to the relaxation oscillation frequencies ω_{ro} which had also been observed in the temporal measurement. It is found that the peak frequency shifted toward higher frequency as increasing the pump power. In generally, a YDF laser oscillator acts as quasi three-level laser system, however, we were able to treat the observed relaxation oscillations in the four-level laser system since the YDF laser behaves as almost the four-level laser system in the case of the lasing wavelength being about 1064 nm as described in [40]. Thus, the observed relaxation oscillations was able to be analyzed by the expression (2.3.25) introduced in the previous chapter.

We defined the observed peak frequencies in figure 4.5b as $f_m(r)$. The square of those, $f_m^2(r)$, were plotted as a function of $(r-1)$ as shown in figure 4.6, where the red line indicates the fitting function given by

$$y = ax, \tag{4.1.2}$$

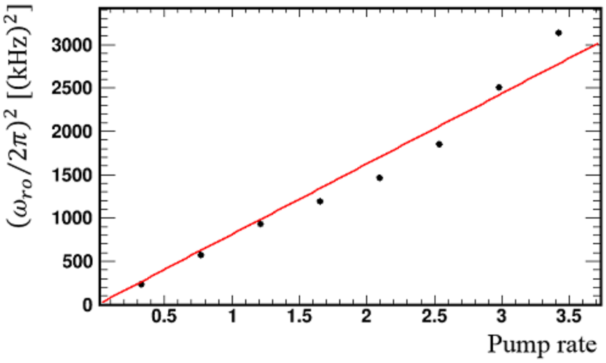

Figure 4.6: The square of measured damping oscillation frequencies and the fitting function of $(\omega_n/2\pi)^2$.

where

$$\begin{aligned} y &\equiv \frac{\omega_{ro}^2}{(2\pi)^2} \sim \frac{\omega_n^2}{(2\pi)^2}, \\ x &\equiv r-1, \\ a &\equiv \frac{\gamma_2\gamma_L}{(2\pi)^2}, \end{aligned}$$

ω_{ro} is the angular frequency of the damping oscillation and defined from equation (2.3.28), ω_n is the natural angular frequency defined from equation (2.3.26), and approximation is came from the relation $\zeta^2 \ll 1$. The γ_2 was about 1 kHz by assuming a typical fluorescence lifetime of the YDF, $\tau_2 = 1$ ms. From equation (2.3.27), therefore, ζ^2 was

$$\zeta^2 = \left(\frac{r\gamma_2}{2\omega_n}\right)^2 = \left(\frac{2\pi r\gamma_2}{2f_m(r)}\right)^2 \sim \left(\frac{1\text{ kHz}}{O(10)\text{ kHz}}\right)^2 \ll 1. \tag{4.1.3}$$

The intra-loop loss on the oscillator was $\alpha_{loop} = -6.4$ dB ($= 0.229$) as described above section. And the decay time constant of the cavity was calculated as $\tau_c = Fl/\pi c = 85.9$ ns. This time constant was larger than the round-trip pass time in the oscillator, τ_L, which was defined by the sum of the optical length of the fiber and the free-space except the cavity. Therefore, we were be able to consider γ_c to be the same as γ_L in equation (2.3.15) and the decay rate was estimated as $\gamma_L =$17.2 MHz. As a result of performing the fit with τ_2 as a free parameter, $\tau_2 = 0.54 \pm 0.02$ kHz was obtained, where the error is a fitting error. This result shows that the estimated fluorescence lifetime was 1.9 ms and that is consistent with the typical fluorescence lifetime of the YDF, 1 ms.

4.1.4 Evaluation of performances of the cavity

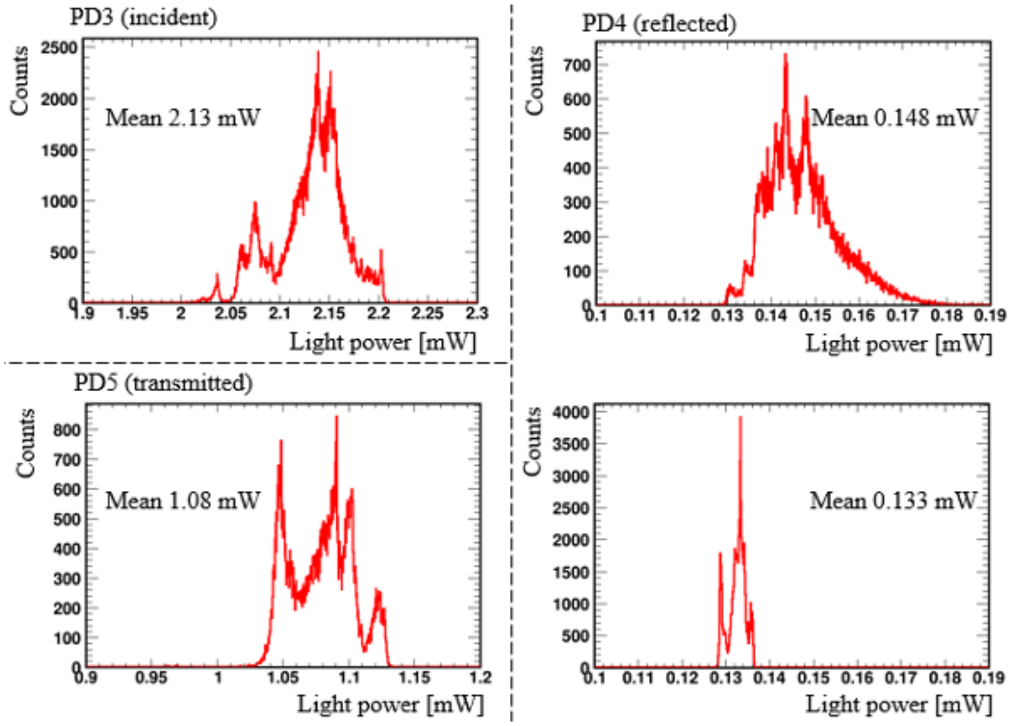

Figure 4.7: Distributions of the measured light power around the cavity.

The laser power balance around the cavity was measured in order to evaluate the performance of the feedback-free cavity with low finesse. Figure 4.7 shows distributions of the power measured at PD3, PD4 and PD5, which correspond to incident, reflected and transmitted laser power, respectively. The power distributions had several peaks indicating that the resonant condition was changing while the system kept the resonance. This power fluctuation was consistent with the mode-hopping behave observed in the laser spectrum. Figure 4.8 shows average powers after correcting the sampling efficiencies of optical samplers at PD3, 4 and 5. The incident, reflected and transmitted power were $P_{in} = 65.4$ mW, $P_{re} = 11.0$ mW and $P_{tr} = 50.4$ mW, respectively.

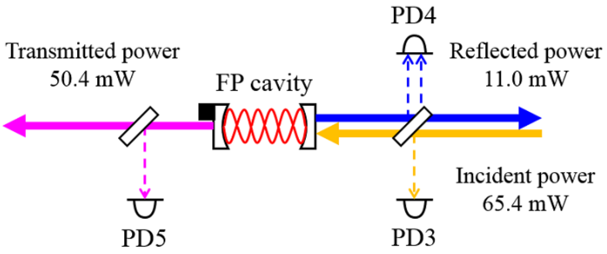

Figure 4.8: The obtained power balance of the intra-loop light around the cavity.

With the effective reflectivity of the cavity mirrors and the obtained average powers around the cavity, the effective transmittance T and the loss $A = 1 - R - T$ of the mirror were calculated by using the relation in figure 2.9:

$$\begin{aligned} T &= 0.80 \pm 0.04 \ \%, \\ A &= 0.04 \pm 0.06 \ \%, \end{aligned}$$

here, the coupling efficiency caused by the difference of the spacial mode between the cavity and the incident light was neglected. As a result, the power enhancement factor of the cavity was obtained as

$$G = \frac{2P_{tr}/T}{P_{in}} = \frac{2T}{(1-R)^2} = 229 \pm 24.$$

The error came from the uncertain of the cavity finesse and the power meter, which had 0.5 % in linearity according to the specification.

The effective power coupling efficiency between the cavity and the incident light, η_{cup}, was estimated by calculating the expected incident power P_{in}^{ex} from the transmitted power:

$$P_{in}^{ex} = \frac{(1-R)^2}{T^2} P_{tr} = 55.6 \ \mathrm{mW}.$$

Therefore,

$$\eta_{cup} = P_{in}^{ex}/P_{in} = 85 \ \%.$$

Since the cavity was well aligned from/to the single mode fibers with the spacial mode matching efficiency of more than 90 % in the experiment, this result may indicate that there were some additional optical loss mechanism originated from the phase difference from the precise resonant condition.

4.2 Development of the high finesse feedback-free optical cavity

4.2.1 High finesse optical resonant cavity

We made a high finesse cavity which consists of two ultra-low loss concave mirrors manufactured by Advanced Thin Films. At first, we measured the transmittances of two mirrors by using the optical setup shown in figure 4.9. The expected transmittance was $O(10^{-6})$, hence the mirrors were mounted on a light proof tube in order to shield stray light from the environment. The wavelength of the incident laser light was 1047 nm and the power was $O(10)$ mW. As a result of the measurement, obtained transmittances, T_1 for mirror M1 and T_2 for mirror M2, were obtained as

$$\begin{aligned} T_1 &= 4.17 \pm 0.02 \text{ ppm}, \\ T_2 &= 3.77 \pm 0.02 \text{ ppm}, \end{aligned}$$

where the errors mainly came from the uncertainty of the linearity of the power meter. The measured transmitted power were $O(10)$ nW and the background optical power was about a few 100 pW in the measurement. The effective transmittance was calculated as

$$T = \sqrt{T_1 T_2} = 3.965 \pm 0.014 \text{ ppm}.$$

Next, the finesse of the cavity was measured by using the cavity ring-down technique. Two mirrors were mounted on a super-inver alloy tube with holders made of aluminum. The distance between two mirrors was $l = 208 \pm 1$ mm that corresponded to the free spectral range of $\nu_{\mathrm{FSR}} = 721.1 \pm 3.5$

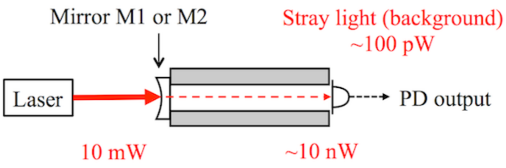

Figure 4.9: A schematic diagram of the transmittance measurement of cavity mirrors. Each power written in figure are the typical measured power.

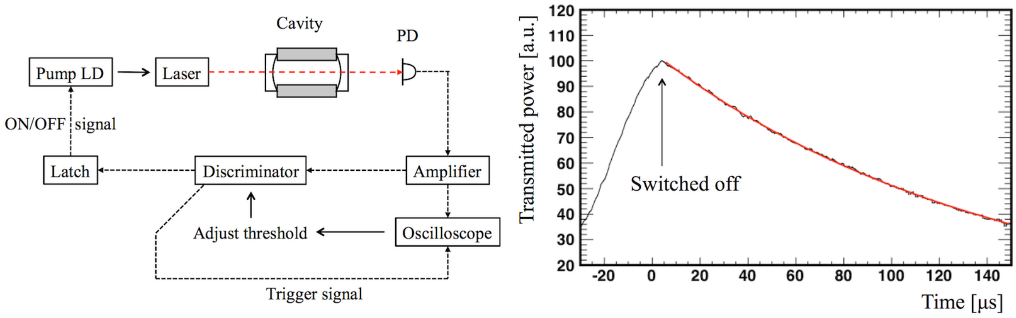

(a)

(b)

Figure 4.10: (a) The schematic diagram of the finesse measurement by using the cavity ring-down technique. (b) The measured ring-down signal and a exponential fitting function.

MHz. Figure 4.10a shows the schematic diagram of the measurement. A fiber laser oscillator with the center wavelength of 1047 nm was used for the incident light source. The falling time of the pump laser diode at turning off was about 10 μs; this decay time did not affect the measurement of the ring-down signal since it was smaller than the expected decay time constant of the cavity. By waiting for the timing that the resonance condition was satisfied accidentally by drift of the cavity length or the laser frequency, the transmitted power built up and the latch circuit activated, and then the ring-down signal was obtained.

The measured decay signal with a exponential fitting function is shown in figure 4.10b. The incident light was turned off at the time indicated “Switched off” in the figure. From equation (2.2.30), the cavity decay time constant and the corresponding linewidth were

$$\begin{aligned}\tau_c &= 142.542 \pm 0.056\ \mu\text{s},\\ \Delta\nu &= 1116.55 \pm 0.44\ \text{Hz}.\end{aligned}$$

With ν_{FSR} and T, the finesse of the cavity, effective reflectivity and effective loss of the mirrors were obtained as

$$\begin{aligned}F &= 645,800 \pm 4,000,\\ R &= 99.9995135 \pm 0.0000030\ \%,\\ A &= 0.900 \pm 0.033\ \text{ppm}.\end{aligned}$$

These results were consistent with the ones expected by the mirror specification.

4.2.2 Construction of a high finesse feedback-free optical cavity

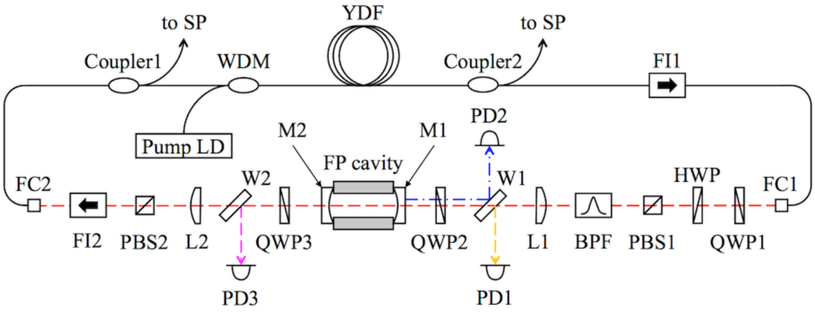

Figure 4.11: A schematic drawing of the optical setup of the feedback-free cavity using the high finesse cavity. The detail is in main text.

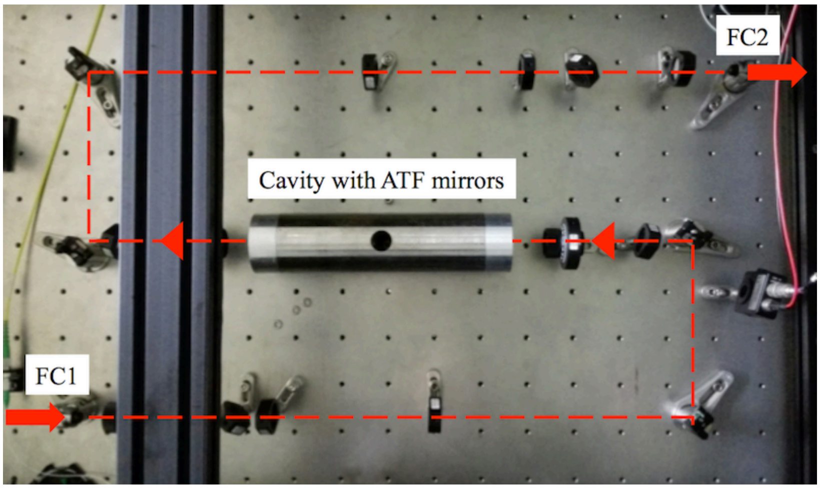

Figure 4.12: A photograph of the cavity and optical components in the free-space. The cavity consisted of a super-inver alloy tube and two ultra-low loss mirrors.

Figure 4.11 shows a schematic drawing of the optical setup of the feedback-free cavity with the high finesse cavity. The setup was almost same as the one for the low finesse case. An amplifier consisted of a single mod YDF of the length of 38 cm and a pump LD. FI1 and 2 are Faraday isolators, Coupler1 and 2 are fiber couplers to sent a part of circulating light to the spectrum analyzer, and FC1 and 2 are the fiber collimator and coupler. HWP and QWP1 are a half wave plate and a quarter wave plate to adjust the polarization of light coming out from the fiber-space. PBS1 and 2 are plate type polarized beamsplitters, whose transition and reflection ratio depended on the wavelength as well as the angle of the devise with respect to the optical axis and acted as low cut-off filters in the system. BPF is an etalon-type band pass filter whose central wavelength was also able to adjust. W1 and 2 are wedge plates to sample a part of intra-loop light to monitor its power. QWP2 and 3 acted as additional optical isolators with two PBSs. The high finesse cavity was aligned with the fundamental spatial mode of the laser light coming from the fiber couplers by using matching lens, L1 and 2.

Figure 4.12 is a photograph of the cavity and optical components on the optical table. It should be noted that all components were set in the air with room temperature, in acoustic shielding box.

Laser oscillation with the band pass filter

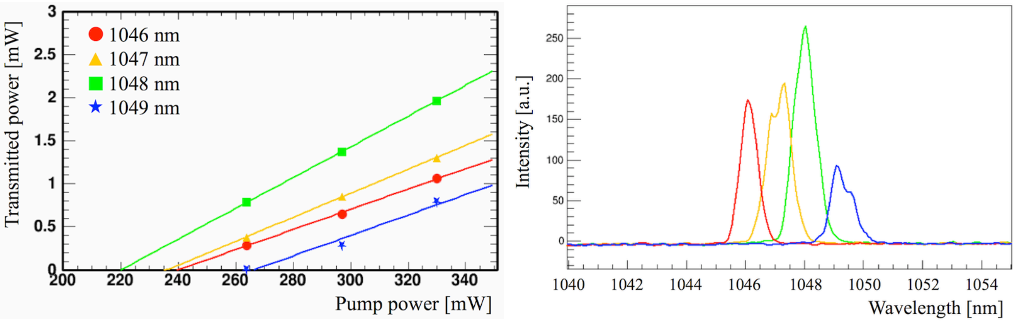

(a)

(b)

Figure 4.13: (a) Observed laser powers as a function of the pump power. (b) Observed power spectra averaged over 10 seconds. Each center wavelength was chosen by the band pass filter.

	1046 nm	1047 nm	1048 nm	1049 nm
Threshold power P_{th}	240 mW	237 mW	220 mW	267 mW
Slop efficiency η_s	0.0117	0.0139	0.0178	0.0117

Table 4.1: Measured threshold powers and slope efficiencies in each chosen wavelength condition.

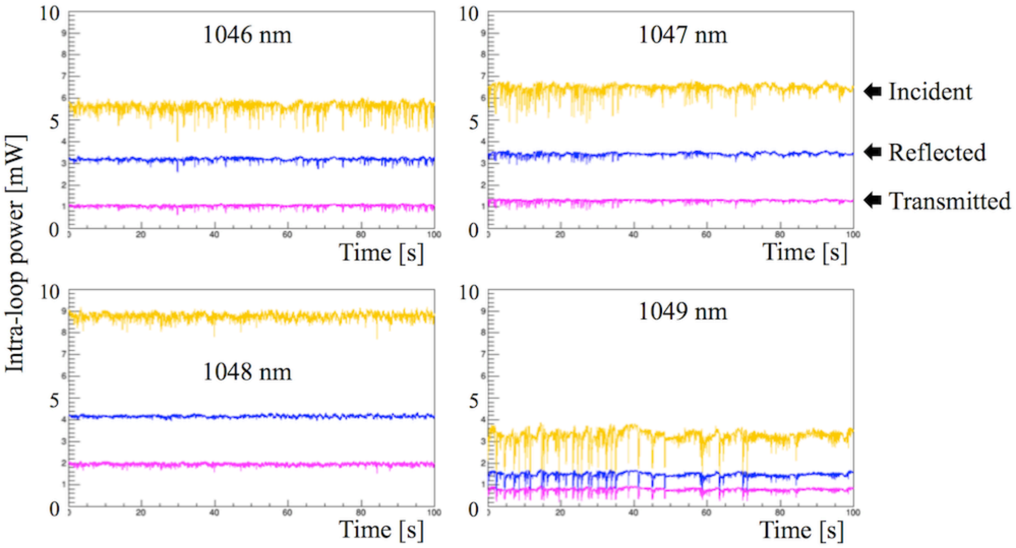

Figure 4.14: Observed time variations of the laser powers around the cavity for 100 seconds. The pump power was set 330 mW.

After adjusting optical components to reduce optical loss and selecting the laser wavelength around 1047 nm which is suitable for the gain of the amplifier, the laser oscillation was observed. Figure 4.13a shows the observed laser power sampled at PD3 as a function of the pump power. Linear lines are fitting functions for each wavelength chosen by the band pass filter. The slopes of the functions and the thresholds of the laser oscillation are summarized in table 4.1. Considering that the gain of the amplifier was almost same in the wavelength range of a few nm, the difference between obtained threshold powers can be attributed to the difference of the optical losses at each chosen wavelength. Furthermore, it is found that those threshold powers were larger than ones of the low finesse case.

Figure 4.13b shows measured power spectra averaged over 10 seconds

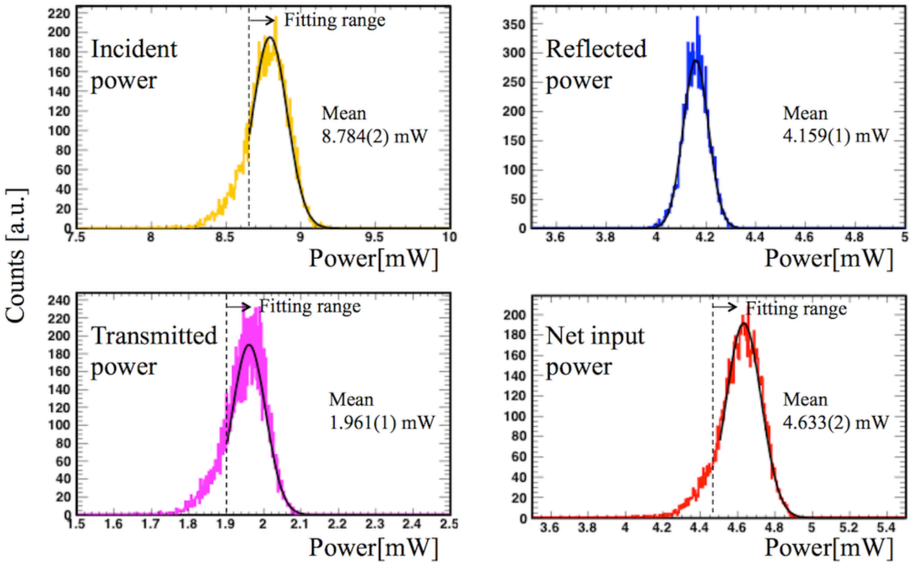

Figure 4.15: Observed power distributions at the wavelength of 1048 nm. Black lines are fitting curves and dot lines indicate fitting ranges.

when the pump power was 330 mW. Each spectrum corresponds to the wavelength chosen by the band pass filter. In a short time-period, each spectrum had a narrower linewidth of less than 0.008 nm; it was determined by the resolution of the spectrometer. And the center wavelength was frequently fluctuating perhaps due to mode hopping, so the linewidth was narrow, however, the lasing wavelength was not stable. Here, the lower limit of the lasing wavelength was determined by the cut frequency of PBSs and the upper limit was determined by the gain-bandwidth of the YDFA.

Figure 4.14 shows time variations of the laser powers around the cavity. The data was for 100 seconds and the pump power was set 330 mW. The incident, reflected and transmitted power measured by PD1, 2 and 3 were corrected for the power sampling ratio of W1 and W2, respectively.

Observed power distributions at the wavelength of 1048 nm were shown in figure 4.15, where the net input power P_{net} was defined by subtracting the reflected power P_{re} from the incident power P_{in} ($P_{net} = P_{in} - P_{re}$). Black lines are fit curves by Gaussian function. The fitting ranges were chosen to avoid the tails of the distributions as indicated in figures. The results of the laser power measurements are summarized in table 4.2.

Light power [mW]	1046 nm	1047 nm	1048 nm	1049 nm
Incident P_{in}	5.694(2)	6.527(2)	8.794(2)	3.295(3)
Reflected P_{re}	3.195(1)	3.437(10)	4.159(1)	1.481(1)
Transmitted P_{tr}	1.069(1)	1.307(1)	1.961(1)	0.7938(8)
Net input P_{in}^{net}	2.497(2)	3.085(1)	4.633(2)	1.816(2)

Table 4.2: The results of the laser power measurements. Each value is means values of the fit.

Laser oscillation without the band pass filter

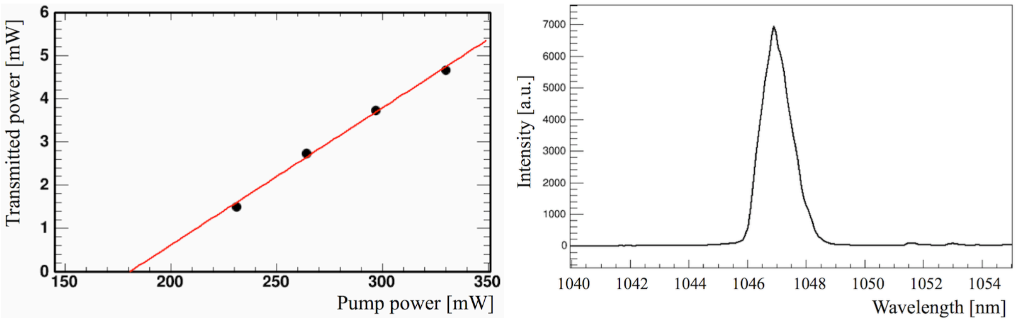

(a)

(b)

Figure 4.16: (a) Observed laser power at PD3 as a function of the pump power in the case of no band pass filter. (b) Observed laser spectrum. The spectrum shape was stable in long time unlike in the case of with the band pass filter.

We also constructed the feedback-free cavity without the band pass filter, and then laser oscillation successfully built up. Figure 4.16a shows the observed laser power at PD3 as a function of the pump power. The red line is the fitting line to the data. The threshold power was obtained as 181 mW and the slop efficiency was 0.0318 (in table 4.3b). It is found that the threshold of the laser oscillation decreased comparing with the case of laser oscillation with the band pass filter.

Figure 4.16b shows the observed laser spectrum. The center wavelength was 1047 nm and the linewidth was 1.3 nm in FWHM. The shape of the spectrum was stable in long time and its linewidth was wider than the one

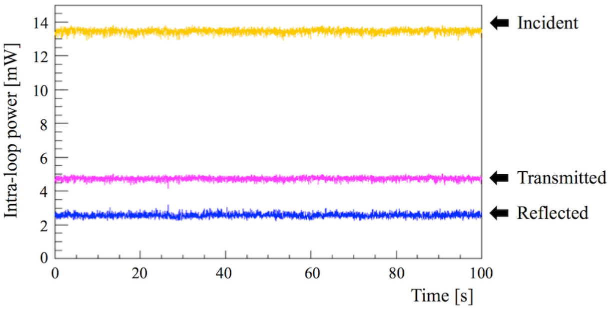

Figure 4.17: Observed time variation of the laser power around the cavity for 100 seconds. The pump power was set 330 mW.

	without BPF
Threshold power P_{th}	181 mW
Slop efficiency η_s	0.0318

(a)

Light power [mW]	without BPF
Incident P_{in}	13.482(1)
Reflected P_{re}	2.556(1)
Transmitted P_{tr}	4.758(1)
Net input P_{in}^{net}	10.916(2)

(b)

Table 4.3: (a) Measured threshold power and slop efficiency in the case of no band pass filter. (b) Measured intra-loop laser powers around the cavity.

for the spectra when the oscillation with the band pass filter. Figure 4.17 shows the time variation of the laser power around the cavity. The data was for 100 seconds and the pump power was set 330 mW. It is found that the laser power was stable and the coupling ratio (reflected power divided by incident power) was better than the one of the results in the case of with the band pass filter. Observed power distributions are shown in figure 4.18. The data were fitted by Gaussian functions (black curves). All distributions had widths of about 5 % in RMS, that was smaller than the widths of about 10 % in the case of with the band pass filter.

From the measurement results which are summarized in table 4.3b, we think that the system laser oscillated as continuous multi mode operation; the stable laser power, relativity large intensity noise and the especially wide linewidth indicate it. When the band pass filter is inserted in the optical loop, the build up of some longitudinal modes would be strongly suppressed.

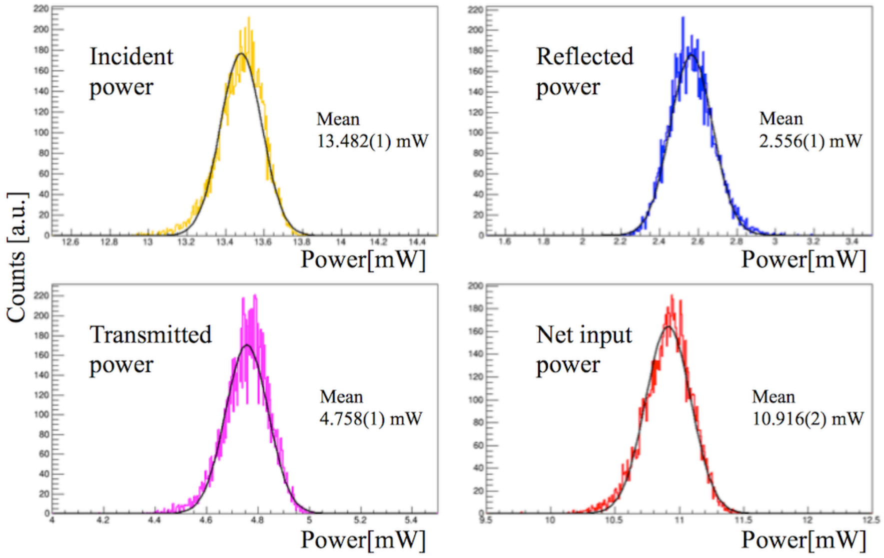

Figure 4.18: The measured power distributions without the band pass filter. Black lines are Gaussian fitting functions.

In the case of with the band pass filter described above section, the laser oscillation would have been forced to operate as single-mode-like (or in a few number of longitude modes) by the filter, and actually such phenomena was observed.

Robustness of the laser storage in multi mode operation

In generally, a single mode operated laser is weak against disturbance and often mode-hops. On the other hand, a laser oscillator in multi mode operation is great stable in its intensity. Therefore, it is expected that the feedback-free cavity in multi mode operation (in the case of no band pass filter) would also have good robustness.

Figure 4.19 shows the display of an oscilloscope which monitored the laser power from PD3. Since the cavity was laser oscillating in multimode operation, a certain constant optical power with some intensity noise was observed. In order to understand its robustness, we hit the cavity body to stop the laser oscillation. The dip signal in figure 4.19 indicates a moment that the oscillation stopped, in other words, the resonant condition was broken. However, the oscillation recovered automatically quickly as shown

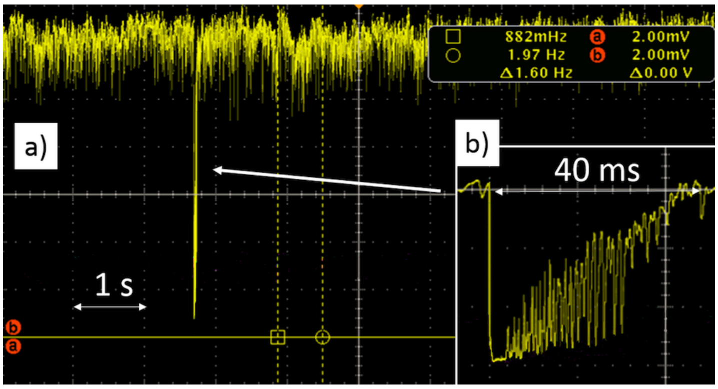

Figure 4.19: (a) The laser power was fell out at the impact, however, recovered soon. (b) The recovery time of 40 ms was consistent with a damping time of the mechanical vibration.

in figure 4.19 (b); the fall time was about 140 μs which was consistent with the decay time constant of the cavity, and the recovery time of 40 ms was consistent with a damping time of the mechanical vibration of the cavity body. It is clearly evident the feedback-free cavity had the good stability against external disturbances.

4.2.3 Evaluation of the system performance

The intra-cavity power P_{cav} and the power enhancement factor G were evaluated. From the transmittance of the end mirror T_2 and the measured transmitted power P_{tr}, those were calculated as

$$P_{cav} = 2P_{tr}/T_2, \tag{4.2.1}$$

$$G = P_{cav}/P_{in}, \tag{4.2.2}$$

where the transmittance was $T_2 = 3.77 \pm 0.02$ ppm as introduced in previous section. The results of the calculation are summarized in table 4.4. Errors mainly resulted from the linearity uncertainty of the power meter of 0.5 %.

The stored laser power in the multi-mode oscillation was reached 2.52 kW by only 330 mW pump power. And the enhancement factor was also reached more than 100,000 in all cases of operation. The observed enhancement factor was, however, smaller than the expected ideal value G_{id} which

	Unit	1046 nm	1047 nm	1048 nm	1049 nm	multi mode
P_{cav}	[W]	567(3)	693(4)	1,040(6)	421(2)	2,524(13)
G	[$\times 10^3$]	99.6(5)	106.2(6)	118.3(6)	127.8(7)	187.2(10)

Table 4.4: The results of the intra-cavity power and the power enhancement factor. Each wavelength means the center wavelength chosen by the band pass filter. The right side results indicates the case of no filter.

can be obtained by considering the ideal resonant condition as introduced in chapter 2:

$$G_{id} = \frac{2T}{(1-R)^2} \sim \frac{2F}{\pi} = 411,100 \pm 2,500. \tag{4.2.3}$$

It should be noted that the optical loss at the cavity mirror was including into this estimated ideal factor. The experimental result indicates that the resonance state of the feedback-free cavity had certain phase difference from the exact resonant condition.

4.3 Measurement of the frequency response function

4.3.1 Measurement scheme and setup

We tried to measure the cavity finesse by using the frequency response measuring technique (see section 3.3.3) while the cavity was laser oscillating with self-resonating mechanism in the multi mode operation. In order to modulate the light intensity, we controlled the pump power driving the YDFA. In general, the pump power modulation affects the population inversion in the laser medium and causes chaotic behavior in the laser intensity [41] because of the coupling term in two differential equations (2.3.10) and (2.3.14). To avoid such instability, we had applied sufficiently small modulation in the pump power (or population inversion). After tuning the modulation depth by controlling the driving current to the LD, the modulation depth in the laser intensity was set at about 1 % with respect to

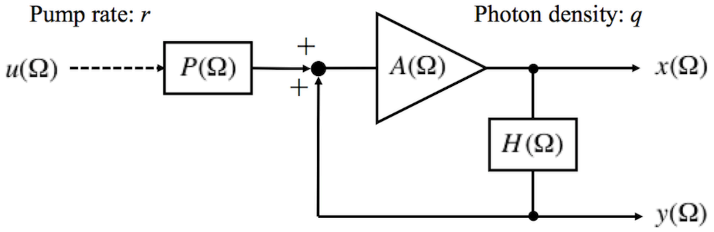

Figure 4.20: A conceptual diagram of the pump power modulation scheme. When the depth of the modulation is small enough, this scheme is same as the intensity modulation technique described in section 3.3.3.

the steady-state laser intensity. Then we were able to treat transmutation of the modulation signal as a liner equation of the photon density q as like equation (2.3.25).

Figure 4.20 shows a conceptual diagram of the frequency response function measurement by using the pump power modulation method. The input modulation signal $u(\Omega)$ of the pump rate r is applied to the closed loop system of the photon density q via the transfer function of $P(\Omega)$, where the modulation angular frequency Ω is sufficiently smaller than the free spectrum range of the cavity. $x(\Omega)$ and $y(\Omega)$ corresponds with the incident and transmitted intensity of laser light. It should be noted that the light payed attention here is not the total intensity but the sideband component; its optical frequency would be $\omega_c \pm \Omega$, where ω_c is the center angular frequency of the laser, and Ω is the modulation angular frequency. $H(\Omega)$ is the transfer function of the cavity and $A(\Omega)$ is unknown transfer function. The transfer function for x/u and y/u can be written as

$$\frac{x}{u} = P\frac{A}{1-AH}, \tag{4.3.1}$$

$$\frac{y}{u} = P\frac{AH}{1-AH}. \tag{4.3.2}$$

From these equations, we obtain

$$\frac{y}{x} = \frac{PAH}{PA} = H. \tag{4.3.3}$$

This relation shows that one can obtain the transfer function $H(\Omega)$ by measuring the response functions of $x(\Omega)$ and $y(\Omega)$.

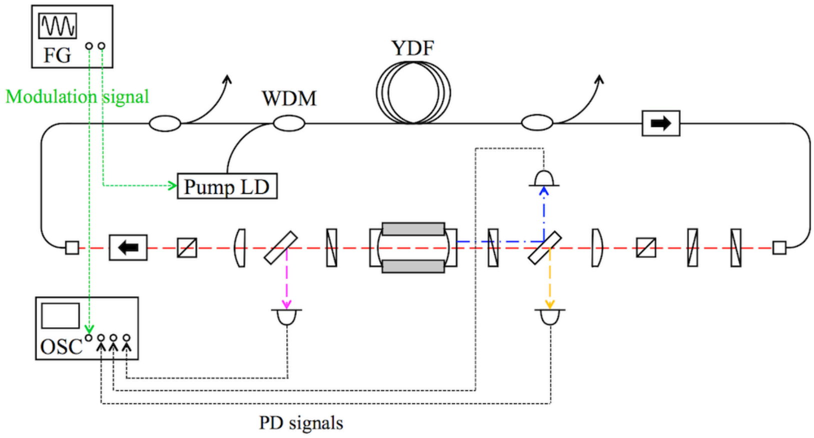

Figure 4.21: A setup drawing of the response function measurement by using the pump power modulation method.

Figure 4.21 shows the setup drawing of the response function measurement. The feedback-free cavity was laser oscillating in multi mode operation with pump power of 330 mW. The electrical current driving the pump LD was modulated by using the sine wave signal generated from a function generator (FG) with the modulation angular frequency of Ω. The modulation bandwidth was up to 10 kHz (the bandwidth of LD was a few MHz). The modulation depth was set to become 1 % at low frequency limit in the laser power. The time variation of the incident power, P_{in} and the transmitted power P_{tr} were measured by PDs with an oscilloscope. Observed time variation of the PD signal was composed of the DC component and the AC component; the DC corresponded with the steady-state light power or carrier light power and the AC corresponded with sideband light power. The AC signals of the incident and transmitted light gave the data sets of the response of $x(\Omega)$ and $y(\Omega)$.

4.3.2 Result of the finesse measurement

Figure 4.22 shows the response function of $y(f)/x(f)$. The red line is the fitting function of a first-order low pass filter expressed as

$$|H(f)| = \frac{\eta_0}{\sqrt{1+(f/f_c)^2}}, \tag{4.3.4}$$

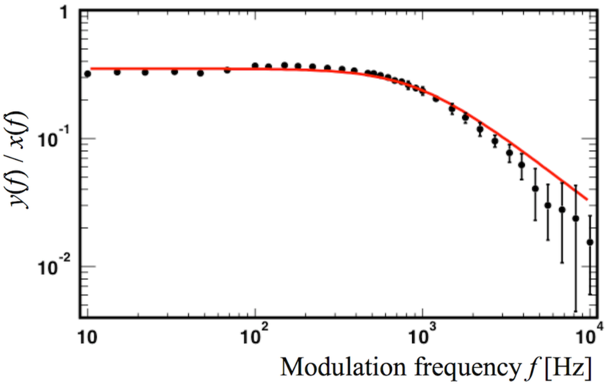

Figure 4.22: Obtained response function of $y(f)/x(f)$. The red line is a fitting function. The detail is in the main text.

where η_0 and f_c are fitting parameters. The cut-off frequency f_c has the relation with the resonance linewidth of the cavity:

$$\Delta\nu = 2f_c. \tag{4.3.5}$$

From this linewidth, we can introduce the *effective finesse*, F_{eff}, which includes performance of the self-resonating mechanism. The results of the measurement and calculation are summarized as below:

$$\begin{aligned}\eta_0 &= 0.351 \pm 0.002,\\ f_c &= 914 \pm 23 \text{ Hz},\\ F_{\text{eff}} &= 394,500 \pm 10,100.\end{aligned}$$

The obtained *effective finesse* was smaller than the finesse obtained by using the cavity ring-down technique in section 4.2.1.

4.4 Relaxation oscillations

In the case of the high finesse cavity, it is difficult to observe relaxation oscillations in the time variation of the light intensity since the long cavity decay time constant gives the damping ratio ζ close to 1. However, the natural angular frequency ω_n and more parameters in relaxation oscillations can be measured by modulating photon density or laser intensity in the laser oscillator [42]. This frequency-domain measurement was just same as the measurement described in before section; the desired response of the photon density Δq in equation (2.3.25) agrees with the obtained $y(f)$ in figure 4.20.

Figure 4.23 shows the measured data set of $y(f)$ as a function of the modulation frequency. The red line is a fitting function of the second-order low pass filter that is written as

$$F(f) = \frac{K}{\sqrt{\left[1 - \left(\frac{2\pi f}{\omega_n}\right)^2\right]^2 + \left[2\zeta\left(\frac{2\pi f}{\omega_n}\right)\right]^2}}, \tag{4.4.1}$$

where K is a normalization factor. This fitting function corresponds with the solution of the damping oscillation, equation (2.3.25). As a result of the fit, the normalization factor K, the natural angular frequency ω_n, and the damping ratio ζ were obtained as

$$\begin{aligned} K &= 399 \pm 2, \\ \omega_n &= 4.96 \pm 0.08 \text{ kHz}, \\ \zeta &= 0.586 \pm 0.009. \end{aligned}$$

With the experimental pump rate

$$r = \frac{330 \text{ mW}}{181 \text{ mW}}, \tag{4.4.2}$$

and equation (2.3.26) and (2.3.27), the decay rates γ_2 and γ_L were calculated as

$$\gamma_2 = 3.2 \text{ kHz},$$
$$\gamma_L = 9.4 \text{ kHz},$$

and the inverse of γ_2 was

$$\tau_2 = \frac{1}{\gamma_2} = 0.31 \text{ ms}.$$

This obtained decay time constant τ_2 is consistent with the magnitude of the order of the typical fluorescence lifetime of the YDF (~ 1 ms), however,

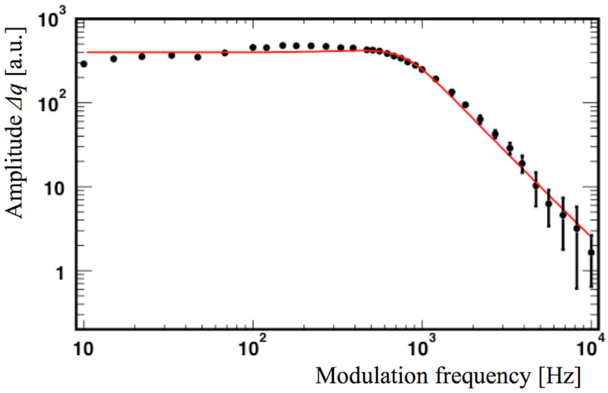

Figure 4.23: Observed response of the transmitted sideband light power, $y(f)$ as a function of the modulation frequency. The red curve is a fitting function of the second-order low pass filter.

it is shorter than the result in the case of low finesse (1.9 ms). The decay rate of the laser cavity γ_L is expressed by equation (2.3.15),

$$\gamma_L = \frac{-\ln \alpha_{\mathrm{loop}}}{\tau_L}. \tag{4.4.3}$$

Assuming that the τ_L is same as the cavity decay time constant, $\tau_c \sim 140$ μs, which was the time constant measured by using the cavity ring-down technique as described before section, the optical loss in the optical loop α_{loop} was estimated as -5.8 dB.

4.5 Discussion

The experimental results shows that the self-resonating mechanism is capable of very stable laser storage for high finesse cavities. The obtained power enhancement factor achieved more than 100,000 and the storage optical power was 2.5 kW with 330 mW pump power. The laser power had relatively large intensity noise, however the mean of the lasing power was quite stable. That stability was also shown in measurement results of relaxation oscillations (figure 4.23). The photon density in the feedback-free cavity had vibration isolation against disturbance.

One of the questions to this system is why the cavity finesse was observed to be small in the laser storage or laser oscillation. The finesse is originally defined only from the reflectance of the cavity mirror and gives the enhancement factor of optical power or the interaction length in the exact resonance condition. On the other hand, the *effective finesse* was introduced from the enhancement factor of the interaction length, which has a relation with the decay time constant of the transmitted light. In that sense, the obtained finesse by using the cavity ring-down technique may also be better to be called the *effective finesse*, however, there is difference between the cavity ring-down technique and the frequency response function technique. In the later case, the laser light is continually irradiating the cavity. The time variation of the phase difference in the resonance causes the Doppler shift on the optical frequency of the intra-cavity light [43, 44]. Without the incident light, there is no effect on the intensity of the transmitted light (ring-down signal), however, the presence of the incident light field causes some intensity modulation caused by the interference between the incident and transmitted light (see Appendix B).

In figure 4.21, the instantaneous frequency of the incident light would have been different from the intra-cavity light since the incident light was coherent light for the past light in the cavity. It can be presumed that the inconsistency between the result of the cavity ring-down technique and the result of the frequency response technique is caused by intensity modulation due to the interference between incident light and transmitted light. We could not analyze this matter in more detail in this experiment since the laser oscillation in multi mode operation gives only the average intensity of the light of a myriad of longitudinal modes. The same situation occurred in the case of with the band pass filter since the central lasing wavelength was frequently mode-hopping.

The result of relaxation oscillations is also measurement which gives information on the cavity finesse as the decay time constant of a laser cavity τ_L. However, as we have seen, the measurement result showed that the decay rate of the fluorescence γ_2 was different from the fluorescence lifetime of a YDF and the result in the low finesse case. Since the fluorescence lifetime is specific character of the atoms in a YDF, the value does not change depending on the configuration of the optical setup. According to reference [40], the YDF laser oscillator operating at the lasing wavelength of 1047 nm does not follow the strict four level system. For detailed verification, we will have to consider other models of relaxation oscillations in quasi-three level systems. Furthermore, it will be necessary to improve the experimental accuracy: change of the lasing wavelength, use of other cavity finesses, use of different laser medium, etc.

Chapter 5

Conclusion

We successfully demonstrated the highly stable operation of a feedback-free optical cavity with the self-resonating mechanism. In this work, the highly stable operation with the effective finesse of $394,000 \pm 10,000$, which is two orders of magnitude higher than our previous study [17], was achieved. The stored power in the cavity was 2.52 ± 0.13 kW with stability of 1.7 % and the power enhancement factor of the cavity was $187,000 \pm 1,000$. The results showed a scheme to overcome an issue to construct a high finesse optical resonant cavity since required precision for the cavity length to stabilize the cavity with this effective finesse and the power stability is about 0.16 pm, which could only been achieved with a sophisticated feedback control system. The system showed a continuous operation of more than two hours with the power fluctuation of 1.7 %, showing high robustness against environmental disturbances.

This study showed the possibility of realizing a high finesse cavity without a sophisticated active feedback system. It is highly useful for applications, such as photon sources by laser Compton scattering, cavity enhanced absorption spectroscopy (CEAS) [46–48] or the measurement of vacuum magnetic birefringence [49, 50]. In later two applications, highly large enhancement of the optical interaction length is strongly required, however, the narrow laser linewidth is not required. In particular, we can directly apply the cavity ring-down technique or the response function technique to the CEAS since it obtains information from the change of finesse by trace elements, independent of the power stability.

For the practical use for the photon sources by laser Compton scattering, the mode-locked laser oscillation is necessary to obtain the desired peak power density. We are currently pursuing the realization of the mode-locking in a feedback-free cavity. Issues such as the development of optical components that will be durable for high-power transport and storage, particularly high-damage threshold mirrors, have yet to be overcome but are expected to be developed in optics communities, once the usefulness of this technique is successfully demonstrated.

Appendix A

A.1 Optical ray matrices

According to the Farmer's law, light passes through arbitrary two positions with minimum travel time as an optical ray. The ray is written by an optical ray vector R with the transverse position r and the divergence angle r' with regard to an optical axis:

$$R = \begin{pmatrix} r \\ r' \end{pmatrix}. \tag{A.1.1}$$

Consider an incident ray vector R_{in} enters an optical system and the corresponding output ray vector R_{out} exits the system, the optical system can be expressed by a 2×2 matrix:

$$R_{\text{out}} = \begin{pmatrix} A & B \\ C & D \end{pmatrix} R_{\text{in}}, \tag{A.1.2}$$

where A, B, C, D are matrix elements. This matrix is called as the ray matrix and its matrix elements depends on each optical component; for free propagation of distance d, the ray matrix is given by

$$D = \begin{pmatrix} 1 & d \\ 0 & 1 \end{pmatrix}; \tag{A.1.3}$$

for focus or defocus the rays by using a lens with a focal length of f, the ray matrix is given by

$$F = \begin{pmatrix} 1 & 0 \\ -1/f & 1 \end{pmatrix}. \tag{A.1.4}$$

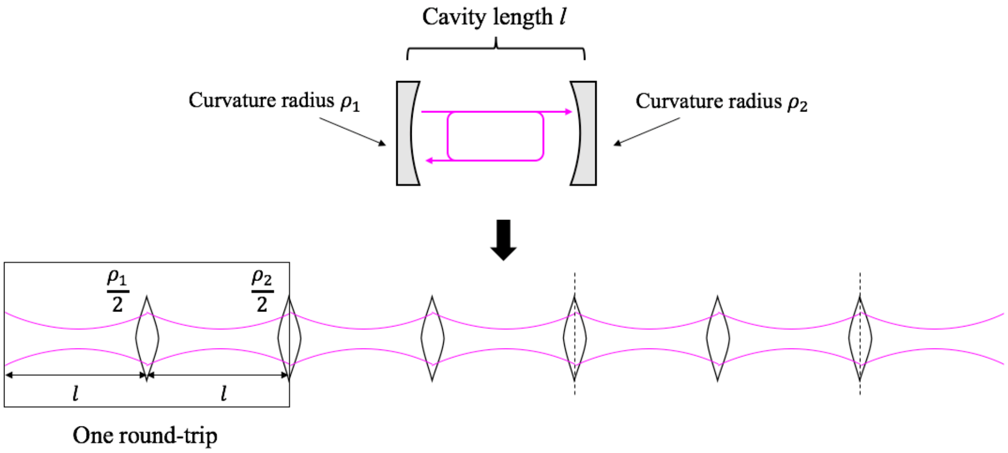

Figure A.1: The equivalent lens guide optical system with regard to a Fabry-Pérot cavity. The box shows a component of the one round-trip propagation.

We can express a two-mirror optical resonant cavity (Fabry-Pérot cavity) as the periodic sequence of lens guide optical system using above ray matrixes of D and F. Figure A.1 shows the conceptual diagram of it, where $\rho_{1,2}$ are the curvature radii of each mirror, l is the distance between two mirrors, the cavity length. The ray matrix of a spherical mirror is the same as the matrix of a lens except that the focal length f is replaced a half of the curvature radius, $f = \rho/2$ [51]. The light propagation in the cavity will be given by the infinite product of following one round-trip ray matrix in the loss less case:

$$M = \begin{pmatrix} 1 & 0 \\ -2/\rho_2 & 1 \end{pmatrix} \begin{pmatrix} 1 & l \\ 0 & 1 \end{pmatrix} \begin{pmatrix} 1 & 0 \\ -2/\rho_1 & 1 \end{pmatrix} \begin{pmatrix} 1 & l \\ 0 & 1 \end{pmatrix}. \tag{A.1.5}$$

Assuming the symmetric cavity, $\rho = \rho_1 = \rho_2$, the minimum spot of the light beam would be at the center of the cavity. Setting the start position of the light propagation at that center, one round-trip ray matrix of the cavity in equation (A.1.5) can be modified as

$$M' = \begin{pmatrix} 1 & l/2 \\ 0 & 1 \end{pmatrix} \begin{pmatrix} 1 & 0 \\ -2/\rho & 1 \end{pmatrix} \begin{pmatrix} 1 & l \\ 0 & 1 \end{pmatrix} \begin{pmatrix} 1 & 0 \\ -2/\rho & 1 \end{pmatrix} \begin{pmatrix} 1 & l/2 \\ 0 & 1 \end{pmatrix}. \tag{A.1.6}$$

A.2 Gaussian beams

By paraxial approximating the wave equation of electromagnetic waves around the z axis, which is the optical axis, we obtain the two-dimensional Schrödinger equation as follows:

$$\frac{\partial^2 u}{\partial x^2} + \frac{\partial^2 u}{\partial y^2} + 2ik\frac{\partial u}{\partial z} = 0, \tag{A.2.1}$$

where u is the amplitude of the light field; $k = 2\pi/\lambda$ is the wave number of light, where λ is the wavelength of light. This equation has set of solutions which is generally called as high-order Gaussian modes; Hermite-Gaussian modes, Laguerre-Gaussian Modes, and so on [51, 52].

Characteristic of the lowest or fundamental mode of solutions of equation (A.2.1) is the most important to describe the propagation of the paraxial optical wave since high-order modes can be derived from the fundamental mode by utilizing the ladder operator in operator methods [53]. The normalized form of the fundamental mode is given by [51]

$$\overline{u}(r, z) = \frac{w_0}{w(z)} \exp\left\{-i[kz - \eta(z)] - \frac{r^2}{w^2(z)} + i\frac{kr^2}{2R(z)}\right\}, \tag{A.2.2}$$

where

$$\eta(z) = \tan^{-1}\left(\frac{\lambda z}{\pi w_0}\right) \tag{A.2.3}$$

is the Guoy phase, $w(z)$ is the radius size where the light field amplitude becomes $1/e$ from the optical axis, w_0 is its minimum value chosen at $z = 0$, and $R(z)$ is the curvature radius of the wavefront of the light beam. $w(z)$ and $R(z)$ are functions of λ and w_0 defined as follows:

$$w(z) = w_0\sqrt{1 + \left(\frac{\lambda z}{\pi w_0^2}\right)^2}, \tag{A.2.4}$$

$$R(z) = z\left[1 + \left(\frac{\pi w_0^2}{\lambda z}\right)^2\right]. \tag{A.2.5}$$

The light propagation formed by the fundamental mode, the Gaussian beam, obeys these functions as shown in figure A.2. The position where the radius size becomes the minimum w_0 is called the beam waist. At the waist,

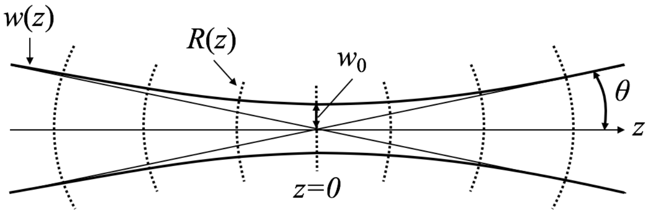

Figure A.2: Propagation of the Gaussian beam. An origin of the propagation direction z is set to the waist position.

the Gaussian beam has infinite wavefront curvature that is a flat wavefront. Furthermore, at positions far enough apart from Rayleigh range, which is defined as

$$z_{\mathrm{R}} = \frac{\pi w_0^2}{\lambda}, \tag{A.2.6}$$

the light beam becomes equal to the spherical wave emitted from the point light source. The divergence angle θ of the beam is given by

$$\tan\theta \sim \theta = \frac{\lambda}{\pi w_0}, \tag{A.2.7}$$

where approximation of tan holds when θ is sufficiently small.

A.3 Gaussian beam in a Fabry-Pérot cavity

The propagation of the Gaussian beam can track using a ray matrix as well as geometric rays. The complex beam parameter, $q(z)$, consisting of $w(z)$ and $R(z)$ is introduced as follows:

$$\frac{1}{q(z)} = \frac{1}{R(z)} + \frac{2i}{kw^2(z)}. \tag{A.3.1}$$

The beam parameter at the waist ($z = 0$) is given by

$$q(0) = -\frac{i\pi w_0^2}{\lambda}. \tag{A.3.2}$$

Before and after the Gaussian beam passes through optical system, the beam parameters change as follows [51]:

$$q_{\mathrm{out}} = \frac{q_{\mathrm{in}}A + B}{q_{\mathrm{in}}C + D}, \tag{A.3.3}$$

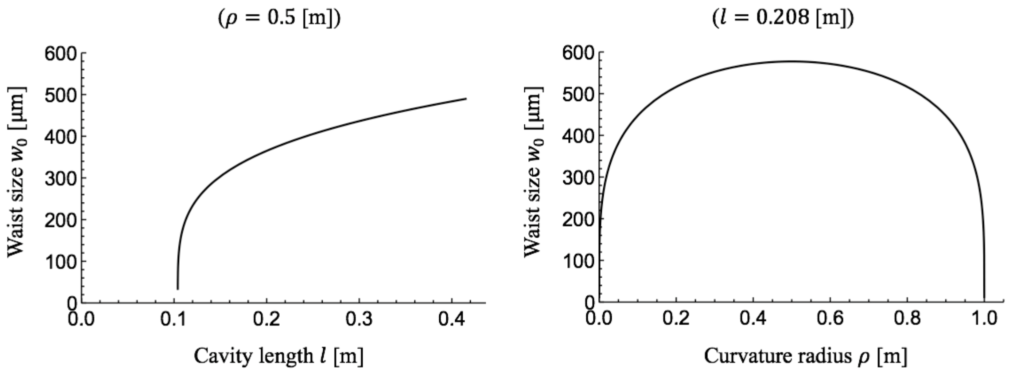

Figure A.3: Plots of the minimum focal spot size w_0 as a function of the curvature radius ρ with the fixed cavity length (left side) and a function of the the cavity length l with the fixed curvature radius (right side).

where $q_{in,out}$ are beam parameters of the incident and output beam, and A, B, C, D are matrix elements of this system.

Let's consider the propagation of the Gaussian beam in a symmetric Fabry-Pérot cavity. The stable Gaussian mode of the cavity is obtained from following self-consistent relation:

$$q = \frac{Aq + B}{Cq + D}. \tag{A.3.4}$$

Taking into account the the condition on the determinant, $AD - BC = 1$, solution of this equation for $1/q$ is

$$\frac{1}{q} = \frac{D - A}{2B} \pm i\frac{\sqrt{4 - (D + A)^2}}{2B}. \tag{A.3.5}$$

Thus, mode shape on reference plane is obtained as

$$R = \frac{2B}{D - A}, \tag{A.3.6}$$

$$w^2 = \frac{2\lambda|B|}{\pi\sqrt{4 - (D + A)^2}}. \tag{A.3.7}$$

Substituting the one round-trip matrix (A.1.6) into equation (A.3.7), we obtain the minimum focal spot size of the Gaussian beam in the symmetric Fabry-Pérot cavity. (Note that the wavefront is flat since it is the waist of the Gaussian beam.) Figure A.3 shows the the minimum focal spot size w_0 as a function of the curvature radius ρ with the fixed cavity length (left side) and a function of the the cavity length l with the fixed curvature radius (right side). Here, the wavelength of light, curvature radius and cavity length are chosen 1047 nm, 0.5 m and 0.208 m, respectively. It is found that the spot size can be reduced by bringing the cavity length closer to twice of the curvature radius, however, the cavity cannot confine the light when the curvature radius is smaller than a half of the cavity length. Hence, the achievable focusing size will be limited by the geometric accuracy of the cavity.

Appendix B

B.1 Dynamic characteristics of a Fabry-Pérot cavity

Consider a Fabry-Perot cavity composed of two mirrors, and its light fields as shown in figure B.1. Suppose a is the position of the input mirror surface and b is the position of the end mirror surface, and b changes over time with respect to a; the position of b from an origin $x = 0$ is $x = x'(t)$. L is the initial cavity length which is larger than the variation $x'(t) - L$ of the end mirror. The time interval required for the light to make one round-trip in the cavity is given by

$$T = \frac{2L}{c}. \tag{B.1.1}$$

Let the light entering the cavity be a continuous monochromatic plane wave with the frequency of ω and the amplitude of E_{in}. Here, the initial

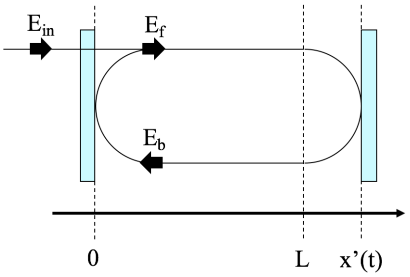

Figure B.1: A Fabry-Perot cavity and its light field. The position of the end mirror b changes over time with respect to a.

cavity length L is an integral multiple of the wavelength of the incident light and it satisfies the following resonance condition:

$$\exp(-i\omega T) = \exp(-2ikL) = 1, \tag{B.1.2}$$

where $k = \omega/c$ is the wave number, and c is the speed of light. The forward electric field E_f and the backward electric field E_b within the cavity immediately after the input mirror surface a are given by [43]

$$\begin{aligned} E_b(t) &= -r_b E_f(t-T)\exp[-2ikx(t-T/2)], && \text{(B.1.3)} \\ E_f(t) &= t_a E_{in} - r_a E_b(t), && \text{(B.1.4)} \end{aligned}$$

where r_a, r_b are reflection coefficients of the input (a) and end (b) mirrors, and t_a, t_b are transmission coefficients of those; $x(t)$ is the variation of b from the initial cavity length L:

$$x(t) = x'(t) - L. \tag{B.1.5}$$

The exponential part on the right side of equation (B.1.3) represents the phase change given by the end mirror after the intra-cavity light travels one round-trip in the cavity. Summarizing two equations (B.1.4) and (B.1.4), we obtained the expression for E_f as

$$E_f(t) = t_a E_{in} + r_a r_b E_f(t-T)\exp[-2ikx(t-T/2)], \tag{B.1.6}$$

and the expression for E_b as

$$E_b(t) = [-t_a r_b E_{in} + r_a r_b E_b(t-T)]\exp[-2ikx(t-T/2)]. \tag{B.1.7}$$

Differential equations of intra-cavity fields

Assuming that the velocity of the end mirror surface b is constant v:

$$x(t) = vt. \tag{B.1.8}$$

When the finesse is sufficiently high, the magnitude of the electric field inside the cavity does not change significantly in the interval T. Thus, we can treat the interval T as a fraction of time, dt, and we can obtain the differential equation of E_f as follows [43]:

$$\begin{aligned}\frac{dE_f(t)}{dt} &\sim \frac{E_f(t+T)-E_f(t)}{T} \\ &= \frac{t_aE_{in}}{T} + \left(r_ar_b\exp\left[-2ikv(t+T/2)\right]-1\right)\frac{E_f(t)}{T}. \quad \text{(B.1.9)}\end{aligned}$$

Since the change in position of the mirror surface b while going through the cavity's resonance point is sufficiently smaller than the cavity length L, the phase change of the electric field given by b can be approximated as follows:

$$\exp\left[-2ikvt\right] \sim 1-2ikvt. \quad \text{(B.1.10)}$$

Substituting this in equation (B.1.9) and eliminating the phase offset, we obtain the following linear differential equation:

$$\frac{dE_f(t)}{dt} \sim \frac{t_aE_{in}}{T} + \left[\frac{r_ar_b-1}{T} - \frac{2ir_ar_bkv}{T}t\right]E_f(t). \quad \text{(B.1.11)}$$

Similarly for E_b, we obtain

$$\begin{aligned}\frac{dE_b(t)}{dt} &\sim -\frac{t_ar_bE_{in}}{T}\exp\left[-2ikv(t+T/2)\right] \\ &\quad + \left(r_ar_b\exp\left[-2ikv(t+T/2)\right]-1\right)\frac{E_b(t)}{T} \\ &\sim -\frac{t_ar_bE_{in}}{T} + \frac{2it_ar_bkv}{T}E_{in}t \\ &\quad + \left[\frac{r_ar_b-1}{T} - \frac{2ir_ar_bkv}{T}t\right]E_b(t). \quad \text{(B.1.12)}\end{aligned}$$

Calculation examples

The transmitted field E_{tr} and reflected field E_{re} from the cavity are given by

$$\begin{aligned}E_{tr}(t) &= t_bE_f(t-T/2), \quad \text{(B.1.13)} \\ E_{re}(t) &= r_aE_{in} + t_aE_b(t). \quad \text{(B.1.14)}\end{aligned}$$

Figure B.2 and figure B.3 show plots of the transmitted and reflected light intensities ,$I(t) = E(t)E^*(t)$, calculated with several values of v, where the

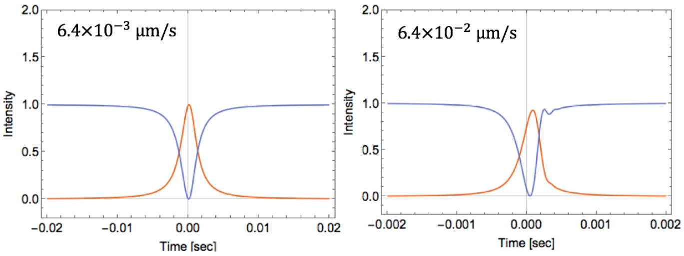

Figure B.2: Red line: transmitted light intensity, blue line: return light intensity. Only one response peak is observed when the mirror speed is slow.

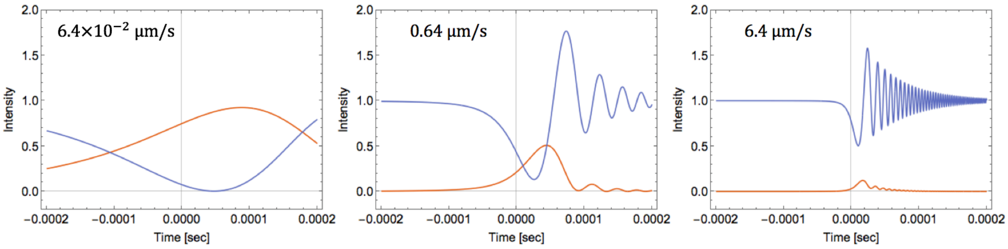

Figure B.3: Red line: transmitted light intensity, blue line: return light intensity. The scales on the horizontal axis are same. Peaks are tilted and the ringing appears at foots of the peaks.

initial cavity length is $L = 1.68$ m, the wavelength is $\lambda = 1064$ nm, the reflectivity of the cavity mirrors is $R = 0.9999$, and the transmittance is $T = 1 - R$; the incident amplitude is set to $E_{in} = 1$.

With the small mirror velocity v, the intensities behave like figure 2.7 and figure 2.8 (see figure B.2). As the velocity gets bigger, the peak is tilted and the ringing starts to appear at the foot of the peak (see figure B.3). Furthermore, it is found that the peak intensity in the transmitted light decreases, and the peak intensity in the reflected light is larger than the incident light intensity.

B.2 Finesse measurement by ringing effects

When the cavity length of a Fabry-Pérot cavity is swept with slow change rate, the symmetrical resonant peaks of the intensity of transmitted light as

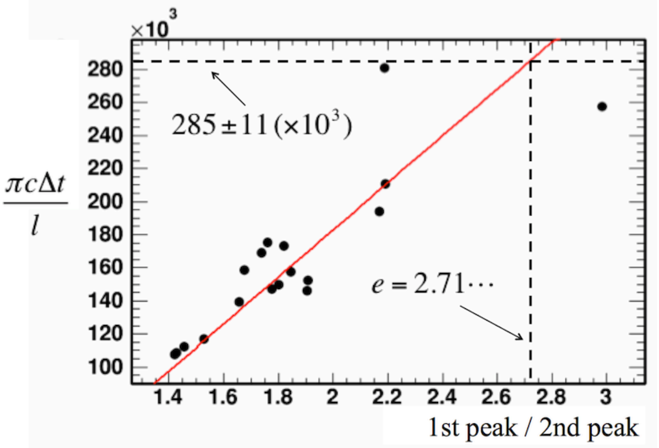

Figure B.4: A result of the finesse measurement with the ringing effect technique. The detail is in the main text.

shown in figure 2.7 are observed. However, when the velocity of the change is quick, the transmitted light exhibits different behavior, depending on the velocity of the mirror, the cavity finesse and the free spectral range of the cavity as shown in the previous section. This phenomenon is understood based on the Doppler effect of the optical frequency in the cavity. The ringing effect can be employed as an application to measure the cavity finesse [54]. In this method, the ratio between the first peak power and the second peak power of the ringing and the time interval Δt between two peaks are measured. Then the finesse is obtained as the value of the variable $\pi c \Delta t / l$ at the ratio being $e = 2.71 \cdots$, where c is the speed of light, l is the cavity length.

With this ringing effect technique, we measured the finesse of a Fabry-Pérot cavity which consisted of two ultra-low loss mirrors provided by LMA; those mirrors had the reflectivity of about 99.999 % according to the specification; the expected finesse and the linewidth were about 300,000 and a few kHz. In the original technique in [54], the ringings were produced by sweeping the cavity length by a piezo-electric actuator with various velocity. In our case, the mirror position was always disturbed by some small mechanical noise due to the narrow linewidth of the cavity and the peaks always had the ringings. We were not able to control the velocity of the

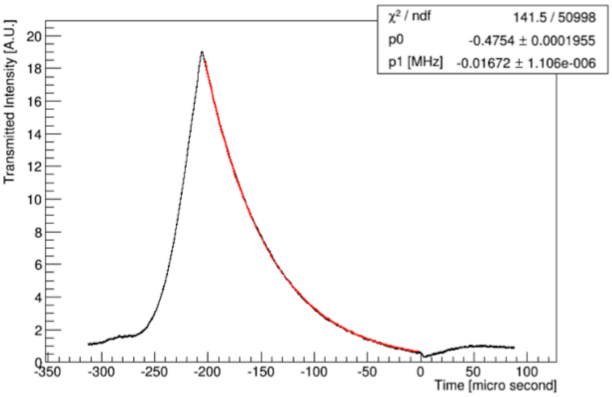

Figure B.5: Observed ring-down signal and the fitting curve.

cavity mirror, however, It was not a problem in this measurement technique.

Figure B.4 shows a result of our measurement. The horizontal axis indicates ratios between the first peak and the second peak powers of each ringing. The vertical axis indicates the variable $\pi c \Delta t / l$. The red line is the fitting line. The obtained finesse was

$$F_{rng} = 285,000 \pm 11,000, \tag{B.2.1}$$

where error was caused by the fitting error. We also measured the cavity finesse by the cavity ring-down technique (see section 3.3.1). The observed ring-down signal and the fitting curve are shown in figure B.5. From this result, the obtained finesse was

$$F_{crd} = 263,000 \pm 4,000. \tag{B.2.2}$$

It is found that the finesse F_{rng} obtained by using the ringing effects was consistent with the finesse F_{crd} obtained by the cavity ring-down technique. Since the ringing effect technique can be used with simple experimental setup, sometimes it would be very effective measuring method especially for high finesse cavities.

Bibliography

[1] W.J. Brown, F.V. Hartemann, “Three-dimensional time and frequency-domain theory of femtosecond x-ray pulse generation through Thomson scattering”, Phys. Rev. ST Accel. Beams 7 (2004) 060703.

[2] K. Sakaue et al., “Observation of pulsed x-ray trains produced by laser-electron Compton scatterings”, Rev. Sci. Intrum. 80 (12) (2009) 123304.

[3] C. Sun, Y.K. Wu, “Theoretical and simulation studies of characteristics of a Compton light source”, Phys. Rev. ST Accel. Beams 14 (2011) 044701.

[4] V. Petrillo et al., “Photon flux and spectrum of γ-rays Compton sources”, Nucl. Instrum. Methods Phys. Res. A 693 (2012) 109.

[5] T. Okugi et al., “Proposed Method to Produce a Highly Polarized e+ Beam for Future Linear Colliders”, Jpn. J. Appl. Phys. 35, 3677 (1996).

[6] T. Omori et al.,“Efficient Propagation of Polarization from Laser Photons to Positrons through Compton Scattering and Electron-Positron Pair Creation”, Phys. Rev. Lett. 96 (2006) 114801.

[7] L. Karim, “Measurement of the positron polarization at an helical undulator based positron source for the International Linear Collider ILC”, PhD, Humboldt-Universität zu Berlin, Mathematisch-Naturwissenschaftliche Fakultät I (2009).

[8] T. Behnke, J. E. Brau, B. Foster, J. Fuster, M. Harrison, J. M. Paterson, M. Peskin, M. Stanitzki, N. Walker, H. Yamamoto, (Editors), “THE

INTERNATIONAL LINEAR COLLIDER Technical Design Report - Volume 1: Executive Summary", www.linearcollider.org

[9] H. Baer, T. Barklow, K. Fujii, Y. Gao, A. Hoang, S. Kanemura, J. List, H. E. Logan, A. Nomerotski, M. Perelstein, M. E. Peskin, R. Poschl, J. Reuter, S. Riemann, A. Savoy-Navarro, G. Servant, T. M. P. Tait, J. Yu, (Editors), "THE INTERNATIONAL LINEAR COLLIDER Technical Design Report - Volume 2: Physics", www.linearcollider.org

[10] C. Adolphsen, et al., (Editors), "THE INTERNATIONAL LINEAR COLLIDER Technical Design Report Volume 3.i: Accelerator R&D", www.linearcollider.org

[11] C. Adolphsen, et al., (Editors), "THE INTERNATIONAL LINEAR COLLIDER Technical Design Report Volume 3.ii: Accelerator Baseline Design", www.linearcollider.org

[12] T. Behnke, J. E. Brau, P. Burrows, J. Fuster, M. Peskin, M. Stanitzki, Y. Sugimoto, S. Yamada, H. Yamamoto, (Editors), "THE INTERNATIONAL LINEAR COLLIDER Technical Design Report Volume 4: Detectors", www.linearcollider.org

[13] For example, Z. Huang and R. D. Ruth, "Laser-Electron Storage Ring", submitted to Phys. Rev. Lett., SLAC-PUB-7556 (1997).

[14] H. Shimizu, S. Araki, Y. Funahashi, Y. Honda, T. Okugi, T. Omori, N. Terunuma, J. Urakawa, M. Kuriki, S. Miyoshi, T. Takahashi, Y. Ushio, T. Hirose, K. Sakaue, M. Washio, P. Guoxi and X. Li, "Photon Generation by Laser-Compton Scattering Using an Optical Resonant Cavity at the KEK-ATF Electron Ring", JPSJ, 78, 7, 074501 (2009).

[15] S. Miyoshi, T Akagi, S. Araki, Y. Funahashi, T. Hirose, Y. Honda, M. Kuriki, X. Li, T. Okugi, T. Omori, G. Pei, K. Sakaue, H. Shimizu, T. Takahashi, N. Terunuma, J. Urakawa, Y. Ushio and M. Washio, "Photon generation by laser-Compton scattering at the KEK-ATF", Nucl. Instr. Meth. A 623, 576-578 (2010).

[16] T. Akagie, et al., "Production of gamma rays by pulsed laser beam Compton scattering off GeV-electrons using a non-planar four-mirror optical cavity", J. of Instr. 7, 001021 (2012).

[17] T. Akagi, S. Araki, Y. Funahashi, Y. Honda, H. Kataoka, T. Kon, S. Miyoshi, T. Okugi, T. Omori, K. Sakaue, H. Shimizu, T. Takahashi, R. Tanaka, N. Terunuma, J. Urakawa, M. Washio, H. Yoshitama, "Development of a three dimensional four mirror optical cavity for laser-Compton scattering", Nucl. Instr. Meth. A 724, 63 (2013).

[18] T. Akagi, S. Araki, Y. Funahashi, Y. Honda, S. Miyoshi, T. Okugi, T. Omori, H. Shimizu, K. Sakaue, T. Takahashi, R. Tanaka, N. Terunuma, Y. Uesugi, J. Urakawa, M. Washio, and H. Yoshitama, "Demonstration of the Stabilization Technique for Nonplanar Optical Resonant Cavities Utilizing Polarization", Rev. Sci. Instr. 86, 043303 (2015).

[19] A. Börzsönyi, R. Chiche, E. Cormier, R. Flaminio, P. Jojart, C. Michel, K. Osvay, L. Pinard, V. Soskov, A. Variola, and F. Zomer, "External cavity enhancement of picosecond pulses with 28,000 cavity finesse", Appl. Opt., 52, 34 (2013).

[20] Y. Honda, H. Shimizu, K. Sakaue, J. Urakawa, N. Sasao and T. Omori, "Photon Target using Self-start Build-up Cavity for Laser Compton Sources", Proc. 7th Annual Meeting of PASJ, 1102 (2010), in Japanese.

[21] G. T. Harvey and L. F. Mollenauer, "Harmonically mode-locked fiber ring laser with an internal Fabry-Perot stabilizer for soliton transmission", Opt. Lett., 18, 2 (1993).

[22] X. P. Cheng, P. Shum, C. H. Tse, J. L. Zhou, M. Tang, W. C. Tan, R. F. Wu and J. Zhang, "Single-Longitudinal-Mode Erbium-Doped Fiber Ring Laser Based on High Finesse Fiber Bragg Grating Fabrv-Perot Etalon", IEEE Phot. Tech. Lett., 20, 12 (2008).

[23] S. H. Parka, V. N. Litvinenkob, W. Tornowc, C. Montgomery, "Spatial distribution and polarization of γ-rays generated via Compton backscattering in the Duke/OK-4 storage ring FEL", Nuc. Inst. Meth. A 475 (2001) 425-431.

[24] W. J. Brown and F. V. Hartemann, “Three-dimensional time and frequency-domain theory of femtosecond x-ray pulse generation through Thomson scattering”, Phys. Rev. ST Accel. Beams 7, 060703 (2004).

[25] C. Sun and Y. K. Wu, “Theoretical and simulation studies of characteristics of a Compton light source”, Phys. Rev. ST Accel. Beams 14, 044701 (2011).

[26] V. Petrillo, et al., “Photon flux and spectrum of g-rays Compton sources”, Nuc. Inst. Meth. A 693 (2012) 109-116.

[27] V. B. Berestetskii, L. P. Pitaevskii, E. M. Lifshitz, “Quantum Electrodynamics, Second Edition: Volume 4”, Butterworth-Heinemann, London (1982).

[28] P. R. Saulson, “Fundamentals of Interferometric Gravitational Wave Detectors”, chapter 6, World Scientific Pub. Co. Inc. (1994).

[29] A. Yariv and P. Yeh, “Photonics, Optical Electronics in Modern Communication, Sixth edition”, Oxford University Press, Inc. (2006) pp. 212 Japanese edition.

[30] M. Rakhmanov, “Doppler-induced dynamics of fields in Fabry-Perot cavities with suspended mirrors”, Appl. Opt., 40, 12 (2001).

[31] M. Rakhmanov, R. L. Savage Jr., D. H. Reitze, D. B. Tanner, ”Dynamic resonance of light in Fabry-Perot cavities”, Phys. Rev. Lett. A 305, 239-244 (2002).

[32] A. Yariv and P. Yeh, “Photonics, Optical Electronics in Modern Communication, Sixth edition”, Oxford University Press, Inc. (2006) pp. 297 Japanese edition.

[33] M. Gorjan, T. North and Martin Rochette, “Model of the amplified spontaneous emission generation in thulium-doped silica fibers”, J. Opt. Soc. Am. B 29, 10 (2012).

[34] R. Paschotta, J. Nilsson, A. C. Tropper and D. C. Hanna, “Ytterbium-Doped Fiber Amplifiers”, IEEE J. of Quant. Electro., 33, 7 (1997).

[35] A. E. Siegman, ”Lasers”, University Science Books, Mill Valley, California, USA (1986) pp. 954-969.

[36] For example, K. Etoh, K. Sekine, M. Watanabe, K. Ito and K. Watanabe, “Development of ultra low loss mirrors for high finesse cavity”, Japan Aviation Electronics Industry, Ltd., 航空電子技報 No.36 (2014), in Japanese.

[37] D. Tatsumi, A. Ueda, “Development of the Ultra-Low Loss Mirrors for Gravitational Wave Detector”, Annualr report of the national astronomical observatory of Japan (ISSN 1346-1192), Vol. 14, 2011, pp. 21.

[38] M. Phelps, L. Zhang, R. Dannenburg, “Drag Wiping with Methanol vs First Contact”, LIGO-T1000137_v3 (2010), www.ligo.caltech.edu

[39] N. Uehara and K. Ueda, “Accurate measurement of ultralow loss in a high-finesse Fabry-Perot interferometer using the frequency response functions”, Appl. Phys. B 61, 9-15 (1995).

[40] L. Orsila and O. G. Okhotnikov, “Three- and four-level transition dynamics in Ybfiber laser”, Opt. Exp. 13, 9, 3219 (2005).

[41] A. N. Pisarchik, A. V. Kir ’ yanov and Y. O. Barmenkov, “Dynamics of an erbium-doped fiber laser with pump modulation: theory and experiment”, Opt. Soc. Am. B, 22, 10, 2811 (2005).

[42] A. E. Siegman, ”Lasers”, University Science Books, Mill Valley, California, USA (1986) pp. 971-973.

[43] M. J. Lawrence, B. Willke, M. E. Husman, E. K. Gustafson and R. L. Byer, “ Dynamic response of a Fabry-Perot interferometer”, Opt. Soc. Am. B 16, 4 ,523 (1999).

[44] M. Rakhmanov, “Doppler-induced dynamics of fields in Fabry-Perot cavities with suspended mirrors”, App. Opt. 40, 12 , 1942(2001).

[45] H. Carstens, N. Lilienfein, S. Holzberger, C. Jocher, T. Eidam, J. Limpert, A. Tunnermann, J. Weitenberg, D. C. Yost, A. Alghamdi, Z. Alahmed, A. Azzeer, A. Apolonski, E. Fill, F. Krausz, I. Pupeza, "Megawatt-scale average-power ultrashort pulses in an enhancement cavity", Opt. Lett., 39, 9, 2595 (2014).

[46] A. O'Keefe and D. A. G. Deacon, "Cavity ring-down optical spectrometer for absorption measurements using pulsed laser sources", Rev. Sci. Inst., 59, 2544 (1988).

[47] G. Gagliardi, H. P. Loock eds, "Cavity-Enhanced Spectroscopy and Sensing" Springer Series in Optical Sciences (2014), ISBN: 978-3-642-40002-5.

[48] K. Stelmaszczyk, P. Rohwetter, M. Fechner, M. Queiβer, A. Czy$\hat{\mathrm{S}}$ewski, T. Stacewicz, and L. Wöste, "Cavity Ring-Down Absorption Spectrography based on filament-generated supercontinuum light", Opt. Exp., 17, 5, 3673 (2009).

[49] F. Della Valle, E. Milotti, A. Ejlli, G. Messineo, L. Piemontese, G. Zavattini, U. Gastaldi, R. Pengo and G. Ruoso, "First results from the new PVLAS apparatus: A new limit on vacuum magnetic birefringence", Phys. Rev. D,s 90, 092003 (2014).

[50] A. Cadene, P. Berceau, M. Fouche, R. Battesti and C. Rizzoa, "Vacuum magnetic linear birefringence using pulsed fields: status of the BMV experiment", Eur. Phys. J. D (2014) 68: 16.

[51] H. Kogelkin and T. li, "Laser beam and resonator", Appl. Opt. 5, 10 (1966).

[52] A. E. Siegman, "Lasers", University Science Books, Mill Valley, California, USA (1986) pp. 642-652.

[53] G. Nienhuis and L. Allen, "Paraxial wave optics and harmonic oscillators", Phys. Rev. A 48, 1 (1993).

[54] J. Poirson, F. Bretenaker, M. Vallet and A. L. Floch, “Analytical and experimental study of ringing effects in a Fabry-Perot cavity. Application to the measurement of high finesses”, Opt. Soc. Am. B 14, 11 (1997) pp. 2811-2817.

公表論文

(1) Feedback-free optical cavity with self-resonating mechanism
Y. Uesugi, Y. Hosaka, Y. Honda, A. Kosuge, K. Sakaue, T. Omori, T. Takahashi, J. Urakawa and M. Washio
APL Photonics **1**, 026103-1-7 (2016); doi: 10.1063/1.4945353

参考論文

(1) Demonstration of the Stabilization Technique for Nonplanar Optical Resonant Cavities Utilizing Polarization
T. Akagi, S. Araki, Y. Funahashi, Y. Honda, S. Miyoshi, T. Okugi, T. Omori, H. Shimizu, K. Sakaue, T. Takahashi, R. Tanaka, N. Terunuma, Y. Uesugi, J. Urakawa, M. Washio and H. Yoshitama
Review of Scientific Instruments **86**, 043303-1-7 (2015); doi: 10.1063/1.4918653

(2) Development of an intense positron source using a crystal-amorphous hybrid target for linear colliders
Y. Uesugi, T. Akagi, R. Chehab, O. Dadoun, K. Furukawa, T. Kamitani, S. Kawada, T. Omori, T. Takahashi, K. Umemori, J. Urakawa, M. Satoh, V. Strakhovenko, T. Suwada and A. Variola
Nuclear Instruments and Methods in Physics Research B, **319**, 17-23 (2014); doi:10.1016/j.nimb.2013.10.025